Spectroscopic Characterization of Interfacial Charge Transfer and Recombination in Polymer/Quantum Dot Blends

Adam E. Colbert

A dissertation

submitted in partial fulfillment of the

requirements for the degree of

Doctor of Philosophy

University of Washington

2016

Reading Committee:

David S. Ginger, Chair

Charles T. Campbell

Brandi M. Cossairt

Program Authorized to Offer Degree:

Chemistry

University of Washington

Abstract

Spectroscopic Characterization of Interfacial Charge Transfer and Recombination in Polymer/Quantum Dot Blends

Adam E. Colbert

Chair of the Supervisory Committee:
David S. Ginger
Department of Chemistry

Considerable research interest in solution-processed semiconductors, including conjugated polymers and colloidal quantum dots, has been primarily motivated by the desire to produce optoelectronic devices using low-cost fabrication methods. Realization of this goal requires both improvements in material properties, and an extensive understanding of the factors regulating device operation and efficiency. This thesis is concerned with spectroscopically probing the fundamental mechanisms of photoinduced interfacial charge transfer in polymer/quantum dot composites, and exploring the role of quantum dot surface chemistry in governing the electronic properties photovoltaic devices. Specifically, we study blends of conjugated polymers with low band gap PbS quantum dots with applications to solar cells and photodetectors.

Quantum dot surface ligands play an important role in mediating the spatial and electronic barrier for charge transfer at the donor/acceptor interface in bulk heterojunction polymer/quantum dot blends. The first part of this thesis explores the effects of postdeposition ligand exchange on the device performance and electronic properties of conjugated polymer composites with PbS quantum dots. We tested a series of ligand exchanges with small bidentate organic molecules, and inorganic iodide ions, and determined that the different treatments influence device performance mainly through changes in open-circuit voltage and fill factor. We found that treatment with 3-mercaptopropionic acid (MPA) yields the highest device efficiencies, and iodide treatment gives the lowest efficiencies. Photoinduced absorption (PIA) experiments showed that MPA treatment results in both greater long-lived polaron populations and longer average polaron lifetimes. We further employed transient photovoltage (TPV) and charge extraction (CE) techniques on solar cell devices to determine that MPA treatment yields greater open-circuit voltages and higher charge carrier densities by promoting longer carrier recombination lifetimes compared to the other ligand treatments. We speculate that these observations are due to differences in carrier mobility and lifetime, in addition to changes in quantum dot energy level alignment relative to the polymer with the different ligands.

Interfacial charge transfer between donor and acceptor materials is a fundamental process for the operation of bulk heterojunction solar cells. The second part of this thesis provides verification of a hole transfer mechanism from photoexcited QDs to the organic host polymer in polymer/quantum dot blends. We used PIA spectroscopy to show that selective excitation of the PbS quantum dot species results in the formation of long-lived charges (polarons) on the polymer chains due to the transfer of photoexcited holes. We also showed that higher photon-energy excitation of both polymer and quantum dot components produces greater charge transfer yields

compared to selective excitation of the quantum dots with lower photon-energy. We hypothesized that either electron transfer is more efficient than hole transfer, or that hole transfer efficiency is wavelength-dependent, suggesting that the excess energy of “hot” (nonthermalized) excitations facilitates hole transfer to the polymer.

Building on these results, we used transient absorption (TA) spectroscopy to investigate the role of pump photon-energy on hole transfer rates in polymer/PbS quantum dot blends through selective excitation of the quantum dot component at two different wavelengths. We showed that higher photon-energy excitation of the blends produces a significantly greater prompt hole transfer yield compared to lower photon-energy excitation, on timescales consistent with carrier cooling rates in the quantum dots. This result provides direct evidence to support the hypothesis that the excess energy of hot carriers in the quantum dots, resulting from excitation with higher photon-energy, facilitates hole transfer to the polymer on subpicosecond timescales. Furthermore, we demonstrate that relaxed carriers on the quantum dots can also transfer to the polymer, at slower rates and with reduced efficiency.

TABLE OF CONTENTS

LIST OF FIGURES

LIST OF TABLES

ACKNOWLEDGEMENTS

I would like to first thank my advisor, David Ginger, for his guidance and support throughout my graduate education. David has provided me with a wealth of opportunities and freedom to learn, and has always been willing to provide direction when I needed it. I also owe much of my success to my undergraduate mentees, Eric Janke, Stephen Hsieh, and Wenbi Wu. I am truly grateful for all of their hard work, and proud of their many accomplishments. Finally, I am indebted to my fellow group members, who have trained and helped me throughout my time at UW: Kevin Noone, Cody Schlenker, Hiro Nagaoka, Liz Strein, Dana Sulas, Ma Fei, Mark Ziffer, Sarah Vorpahl, and Phil Cox.

DEDICATION

To my parents, Patrick and Leigh Colbert

Chapter 1. AN OVERVIEW OF POLYMER/QUANTUM DOT PHOTODIODES AND THE IMPORTANCE OF QUANTUM DOT SURFACE INTERFACES

1.1 THESIS STATEMENT

This dissertation describes significant progress toward understanding the physical interactions between near infrared-absorbing PbS quantum dots and semiconducting conjugated polymers, with applications to next-generation solar cells. Chapter 2 investigates the effects of quantum dot surface chemistry, modified through ligand exchange, on the electronic properties of polymer/quantum dot solar cells. We determine that varying the QD surface ligands primarily affects the device open-circuit voltage and fill factor. We use photoinduced absorption (PIA) spectroscopy to probe the relative long-lived photoinduced charge transfer yields in blends with the different ligand treatments, and further characterize the recombination dynamics in operational devices using transient photovoltage and charge extraction techniques. Both methods indicate that ligand treatments resulting in higher efficiency devices promote longer bimolecular charge carrier recombination lifetimes and greater long-lived carrier populations under open-circuit conditions. The study in Chapter 3 uses PIA to show direct evidence of hole transfer from photoexcited quantum dots to the host polymer, providing verification of this pathway for photocurrent generation. We also observe greater photoinduced charge transfer yields when both polymer and QD components are excited with higher pump photon-energy, suggesting that either electron transfer from the polymer is a more efficient pathway than hole transfer, or that hot (nonthermalized) carriers on the QDs enable more efficient hole transfer. In Chapter 4 we use transient absorption (TA) spectroscopy to demonstrate that excitation of the quantum dots with higher photon-energy produces substantially greater hole transfer yields at prompt (subpicosecond) timescales compared to lower photon-energy excitation. Additionally, we show that hole transfer from relaxed carriers on the quantum dots is a relatively slow, and less efficient process. These results support the premise that the excess energy of hot carriers directly facilitates more efficient hole transfer to the polymer. Finally, Chapter 5 summarizes the overall themes of this work and provides suggestions for future studies.

1.2 MOTIVATION AND BACKGROUND

The aggregate global energy consumption for 2013 is estimated to an average power of ~12.3 TW, and is projected to increase due to population growth and rising demand for energy in developing countries.[1] To accommodate the growing demand for energy and to reduce the environmental impacts of air pollution and carbon dioxide emission, emerging energy technology has increasingly focused on clean, renewable sources of energy. Solar energy is currently one of the most promising renewable energy resources. In the United States, the use of solar has increased by over ten-fold from 1.2 GW in 2008 to 13 GW in 2013.[2] During this time, the levelized cost of energy (LOCE) for solar power has decreased by up to 65%.[3] Established photovolatics based on crystalline and polycrystalline materials such as silicon and CdTe are mature technologies that have continued to improve in efficiency and fall in cost in recent years.[3-4] However, wide-scale implementation of solar technology requires factors other than device efficiency to be taken into account such as energy payback time, environmental impact, and manufacturing cost and scalability. As a result, much of the recent research in solar technology has focused on solution-processable materials such as organic photovoltaics, colloidal nanocrystal quantum dots, and organic/perovskite solar cells. These materials have the potential for wide scale, low-cost implementation using mass production techniques such as roll-to-roll printing, which is where the cost savings of these devices will likely be realized.

Among emerging photovoltaic technologies, colloidal semiconductor quantum dots (QDs) have attracted considerable interest due to their ease of synthesis, solution processability, and tunable electronic properties. Quantum dots are nanometer-scale semiconductor crystals that exhibit size-dependent electronic structure due to the strong confinement of charge carriers in particles with dimensions smaller than the material's Bohr exciton radius. This property allows the quantum dot's absorption and emission profiles to be tailored through particle size, making QDs useful materials for a variety of optoelectronic devices including photovoltaics, light emitting diodes (LEDs), as well as photodetectors and imaging sensors.[5] Lead chalcogenide (PbS, PbSe) quantum dots are of particular interest for use in solar cells because their absorption spectra extend through the near infrared (NIR) spectral region, allowing broader harvesting of solar irradiation.

Organic photovoltaics (OPVs) based on π-conjugated polymers are another promising technology for mass produced photovoltaics. These devices commonly employ bulk heterojunction (BHJ) blends, in which charge carrier generation is driven by interfacial charge transfer between the polymer donor and electron accepting fullerene molecules. While OPV efficiencies have increased considerably in the last two decades due chiefly to advancements of the donor polymer, less emphasis has been placed on exploring alternative acceptor materials. Quantum dots are appealing as acceptor materials in OPVs due to their strong light absorption, size-tunable band gaps, high charge carrier mobilities, and high dielectric constants ($\varepsilon_r \approx 17.2$ for PbS QDs)[6] for screening Coulombic forces between charge carriers. Hybrid blends of conjugated organic polymers with inorganic semiconductor QDs attempt to realize these advantages in BHJ solar cells. However, these polymer/QD devices have experienced limited success compared to their all-organic counterparts, primarily due to difficulty controlling surface charge trapping states on the QDs, and an incomplete understanding of the processes underlying free carrier generation in hybrid systems. This thesis is concerned with studying the fundamental mechanisms governing photoinduced charge generation in hybrid composites of conjugated polymers with PbS quantum dots, as well as investigating the effects of altering the QD surface chemistry on device performance and blend electronic properties. This chapter provides background information on polymer/QD solar cells and a selective overview of QD surface properties.

1.3 ORGANIC AND QUANTUM DOT SOLAR CELLS

1.3.1 *OPV Operating Principles and Performance Metrics*

The operation of organic photovoltaic devices based on π-conjugated polymers differs from devices employing crystalline inorganic semiconductors. Light absorption in inorganic semiconductors leads directly to the formation of free carriers, that can separate at p-n junctions where they can diffuse to their respective electrodes under an applied electric field. In contrast, photon absorption in organic materials forms Coulombically-bound electron-hole pairs, known as excitons, due to their low dielectric constants (ε~3-5).[7] Separation of the electron and hole is facilitated at heterojunctions with an electron acceptor material using a staggered (type II) band alignment. **Figure 1-1** shows a simplified schematic of the processes involved in OPV device operation. First, photon absorption excites an electron in the donor material into the empty lowest unoccupied molecular orbital (LUMO) level, leaving behind a hole in the highest occupied molecular orbital (HOMO), to form an exciton. The exciton must subsequently diffuse to a donor/acceptor interface, at which point the energy level offset between the donor and acceptor LUMO levels is used to drive charge transfer. This energy difference must be sufficient to overcome the exciton binding energy of ~300 meV. The free electron (hole) may then diffuse through the acceptor (donor) material for extraction at the device electrodes.

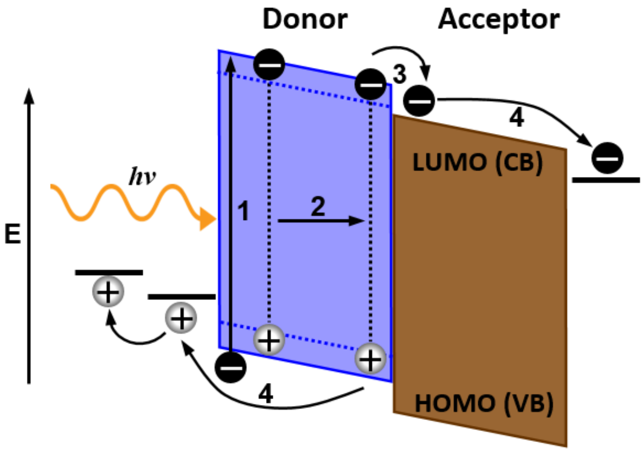

Figure 1-1. Schematic of OPV device operating principles, showing 1) photon absorption, 2) exciton diffusion to a donor/acceptor interfacial site, 3) electron transfer from donor to acceptor, 4) charge extraction to the device electrodes.

Additionally, the exciton diffusion length in semiconducting conjugated polymers is on the order of ~10 nm,[8-9] limited by the low carrier mobilities and fast recombination lifetimes in these materials. However, the absorber layer must be ~100 nm thick in OPVs to absorb sufficient light. This limitation is overcome by the bulk heterojunction (BHJ) design, in which the films are cast from a solution of mixed donor and acceptor, resulting in high interfacial area of intimately mixed donor and acceptor, with nanoscale phase separation on the order of the exciton diffusion length. Once separated, the charge carriers must travel through percolation networks for extraction at their respective electrodes.

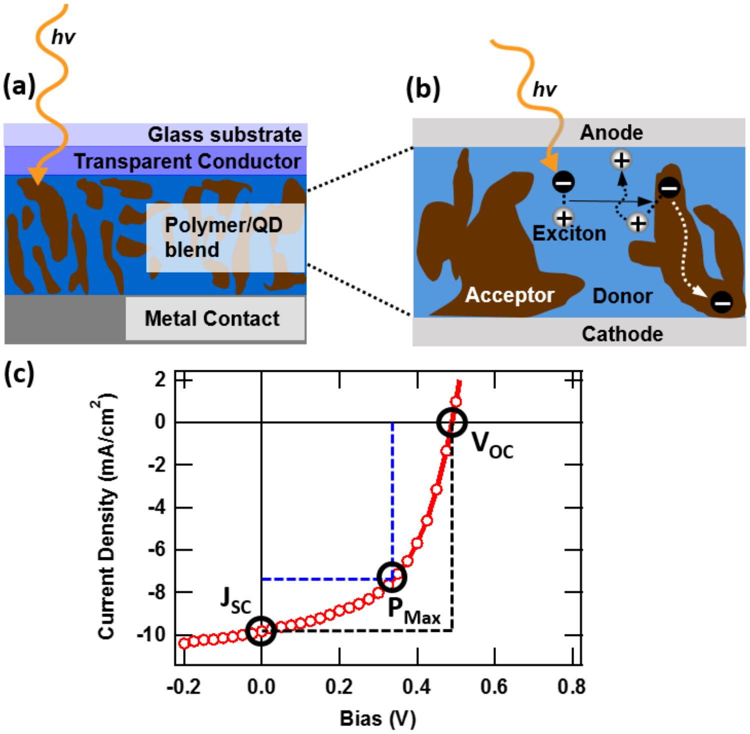

Figure 1-2. a) Schematic of a typical thin film solar cell device structure, b) representation of charge generation and transport in bulk heterojunction blends, and c) standard *J-V* characteristics of a solar cell under illumination, indicating the open-circuit voltage (V_{OC}), short circuit photocurrent (J_{SC}) and maximum power point (P_{Max}) used to calculate fill factor (FF).

Figure 1-2a and b show the typical design and operation of a bulk heterojunction (BHJ) solar cell, in which the absorber layer is sandwiched between a transparent conductor, and a metal back contact. The transparent electrode is typically a conductive oxide such as indium tin oxide (ITO) or fluorine-doped tin oxide (FTO). The surface of this electrode is often modified with the conductive polymer poly(3,4-ethylenedioxythiophene) polystyrene sulfonate (PEDOT:PSS) to smooth the ITO surface and improve hole extraction. Alternatively, the ITO surface can be modified with a layer of high band gap metal oxide such as ZnO or TiO_2 to invert the device polarity. In this case, a higher work function metal such as Au or Ag with a thin electron blocking MoO_3 interlayer is used as the back hole extracting contact. These inverted devices are of interest due to their increased stability to degradation compared to devices using the typical ITO/PEDOT/active layer/Al structure.[10-11] Solar cell performance metrics are commonly acquired by performing current-voltage measurements on devices under simulated solar irradiance with 100 mW/cm^2 intensity, as shown in **Figure 1-2**c. The primary figure of merit is the power conversion efficiency (PCE), descried by the relation:

$$PCE = \frac{J_{SC} \times V_{OC} \times FF}{P_{in}}$$

where P_{in} is the incident illumination power, J_{SC} is the short-circuit photocurrent, V_{OC} is the open-circuit voltage, and FF is the fill factor, which is determined by the ratio of the maximum power point (P_{Max}) to the product of J_{SC} and V_{OC}. The device J_{SC} is related to the number of charges produced in the active layer under no external bias, which depends on the active layer absorption and quantum efficiency (electrons extracted per photons absorbed). The open-circuit voltage of donor/acceptor solar cells is generally related to the energy difference between the donor material's ionization potential (HOMO) and the acceptor material's electron affinity (LUMO).

1.3.2 *Hybrid Polymer/QD Solar Cells*

Hybrid polymer/quantum dot solar cells utilize active layers that are BHJ blends of conjugated polymers with semiconductor QDs. Most of the research on these devices has utilized either CdSe or PbS QDs. Since the early reports of CdSe/polyphenylenevinylene (PPV) solar cells,[12] hybrid device efficiencies have improved by utilizing more efficient donor-acceptor polymers such as poly[2,1,3-benzothiadiazole-4,7-diyl[4,4-bis(2-ethylhexyl)-4H-cyclopenta[2,1-b:3,4-b']dithiophene-2,6-diyl]] (PCPDTBT).[13-14] The QD shape can also influence performance, with CdSe nanorods and tetrapods outperforming spherical QDs by directing electron transport along the principle rod axis, thereby reducing the number of hopping events between nanocrystals prior to charge extraction.[13, 15-16] The enhanced dielectric of QDs compared to organic materials has also been shown to slow the recombination of charge carriers relative to all-organic systems.[17] Many of the highest performing solar cells to date have focused on using low band gap PbS QDs, which have the ability to absorb light into the near infrared to harvest a broader portion of the solar spectrum.[18-19] Polymer/quantum dot solar cell efficiency has also benefitted from improved surface passivation techniques, that enhance interfacial charge transfer, improve carrier mobility in the QD phase, and reduce recombination due to surface trap states.[18, 20-23] While recent progress is promising, polymer/QD devices typically have lower efficiencies than all-organic systems due to the complicated interplay between the polymer and the QD surfaces, especially in regard to incomplete passivation of surface trap states. Further progress with hybrid solar cells is largely dependent upon the ability to balance the factors of quantum dot surface defects, energy level alignment with the donor polymer, and film morphology.

1.4 QUANTUM DOT SURFACE CHEMISTRY

Due to their nanometer scale, quantum dots have inherently high surface area-to-volume ratios. Therefore, many of their electronic properties are determined by the QD surface interface. Quantum dot growth is largely controlled by large Lewis basic surfactant molecules such as oleic acid, oleylamine, or trioctylphosphine. These native ligands form a dense capping layer on the QD surface that maintains particle shape and solubility. However, the bulky native ligands inhibit electronic interaction between QDs and must be exchanged for smaller ligands to decrease interparticle distance and promote electronic coupling among the QDs, for use in electronic devices. Understanding the relationship between QD surface chemistry and electronic properties is therefore critical to using QDs in electronic devices. QD surface composition influences a number factors, such as carrier mobility, trap state passivation, and frontier energy levels. This section provides background on QD ligand exchange strategies and their influence over the resulting device electronic properties.

1.4.1 *Surface Dipole Effects*

The interaction between a ligand and the surface atoms to which it is bound creates a dipole on the quantum dot surface. The strength and direction of this dipole depends on a combination of the ligand's intrinsic dipole moment and the nature and strength of the bond to the QD surface atom(s). The strength and orientation of the surface dipoles can play an important role in the relative energy levels of the QD band edges. Ligand exchange does not alter the QD band gap, but rather shifts the vacuum level, and in turn the valence (VB) and conduction band (CB) levels due to differences in the electrostatic environment of charge carriers that cross the QD-ligand interface.[24] Lewis basic ligands have interfacial dipole moments oriented from the negatively charged ligand toward the positively charged metal atom on the QD surface, causing the energy levels of the QD to shift down in energy. Brown *et al*. demonstrated that in PbS QD films, ligand exchange with iodide ions shifts the QD band edges ~0.9 eV lower compared to ligand exchange with benzenethiol, a difference which is close to the QD band gap of ~1.23 eV.[24] The substantial differences in frontier energy levels can have an important impact on QD device properties, particularly with hybrid polymer/QD devices that rely on staggered heterojunctions for carrier generation. For example, Greaney *et al*. demonstrated that devices using blends of poly-3-hexylthiophene (P3HT) with CdSe QDs had improved V_{OC} when using *tert*-butylthiol ligands compared to pyridine ligands.[21] The high dipole moment of the *tert*-butylthiol ligands was found to shift the QD band edges to give improved band alignment with the host polymer.

1.4.2 *Ligand Exchanges for QD Optoelectronic Devices*

The primary goal of ligand exchanges in QD optoelectronic devices is the replacement of bulky native ligands with small molecules or ions to reduce interparticle spacing in QD films. Excluding other changes, carrier mobility in QD films increases exponentially with decreasing inter-dot distance. For device applications, solid-state ligand treatments have been a common approach to achieve thorough exchange of the native ligands using a wide variety of ligands, without the difficulties of solvent compatibility and particle solubility involved with solution-based exchanges. This process is carried out by depositing thin films of QDs either through spin-coating or dip-coating.[25-26] The films are subsequently exposed to a solution of the new ligand in an orthogonal solvent such as methanol or acetonitrile, resulting in rapid ligand exchange that renders the film insoluble. The volume reduction associated with reducing the inter-dot distance causes significant cracking, motivating the use of a “layer-by-layer” approach in which this process is repeated multiple times with thin layers of quantum dots to fill voids in the previous layer, to yield smooth, uniform films.[27]

Much of the early work with QD solar cells utilized ligand exchange with small bidentate organic molecules with thiol or carboxylic acid head groups, such as 1,2-ethanedithiol (EDT), 3-mercaptopropionic acid (MPA), and benzenedithiol (BDT) molecules. Exchange with halide salts led to even higher efficiencies due to high carrier mobilities and superior passivation from the small ions.[28] The current record efficiencies have been achieved using a thicker layer of iodide-treated QDs topped with a thin layer of EDT-treated QDs.[29-30] The differences in the QD band edge energy due to electrostatic effects allow the EDT-treated layer to serve as a barrier for electrons at the hole extracting contact. Hybrid polymer/QD solar cells rely on the same ligand exchange methods used in all-QD devices. Solution-based ligand exchange strategies have also been explored to avoid some of the drawbacks of film treatments such as film cracking and structural disorder.[18] However, ligand exchange in polymer/QD blends has the added complexity of regulating interfacial charge transfer and recombination between donor and acceptor species, and is investigated in Chapter 2.

Chapter 2. EFFECTS OF LIGANDS ON CHARGE GENERATION AND RECOMBINATION IN HYBRID POLYMER/QUANTUM DOT SOLAR CELLS

Adam E. Colbert, Wenbi Wu, Eric M. Janke, Fei Ma, and David S. Ginger

2.1 INTRODUCTION

Bulk heterojunction (BHJ) blends of inorganic semiconducting quantum dots (QDs) with conjugated polymers are of interest for their potential use in low-cost photovoltaic applications[12, 17, 19-21, 23, 31-38] and infrared-sensitized photosensors.[5, 39] The use of QDs as acceptor materials allow potential advantages over fullerene acceptors such as strong light absorption, tunable band gaps, and high dielectric constants to screen Coulombic attraction between charge carriers.[17, 21, 40] Lead chalcogenide (PbS, PbSe) QDs are of particular interest due to their high carrier mobilities and broad light absorption that can be tailored with particle size for energy conversion through the near infrared (NIR). Despite recent advances in solar conversion efficiency,[9-14, 13] the performance of hybrid polymer/quantum dot solar cells continues to lag behind both their all-organic[11] and all-inorganic[25, 28-29, 41-43] analogs.

As-synthesized QDs are typically capped in long chain alkyl ligands, such as oleic acid or trioctylphosphine oxide, which are necessary to control particle growth and maintain solubility. However, these ligands are electrically insulating and inhibit charge separation at the polymer/QD interface and charge transport between QDs. Efficient charge generation and transport relies upon exchange of the native ligands with small molecules, which decreases interparticle spacing and enhances the dielectric environment and electronic coupling between QDs.[24, 44] The chemical identity of the ligands controls the net surface dipole of the QDs, leading to significant shifts in valence band (VB) and conduction band (CB) energy levels.[24] These energy level shifts must be taken into consideration with hybrid solar cells, in order to maintain a staggered type II heterojunction between the polymer donor and the QD acceptor species.

Quantum dots have intrinsically high surface area-to-volume ratios, making them susceptible to deep trap states from unpassivated surface ions that serve as recombination centers for charge carriers.[40] Recent advances in QD depleted heterojunction solar cells have been realized largely by enhanced surface passivation through advancements in ligand exchange techniques.[28-29, 41-42] Similar surface passivation strategies with organic small molecules such as pyridine have also been shown to improve the performance of lead halide perovskite solar cells through passivation of surface trap states, reducing recombination losses due to non-radiative decay pathways.[45-46] Hybrid solar cells have the added challenge and opportunity managing charge dissociation and recombination at the polymer/QD interface. Much as in all-organic solar cells, rapid charge dissociation with slow recombination is desired. Understanding how to effectively manage this interface through QD surface modification is thus an important part of optimizing hybrid devices, and may provide insights into strategies for managing the balance of dissociation and recombination in other materials systems.

To this end, we examine the effects of post-deposition QD surface modification on photocarrier recombination in hybrid composites of poly((4,8-bis(octyloxy)benzo(1,2-b:4,5-b')dithiophene-2,6-diyl)(2-((dodecyloxy)carbonyl)thieno(3,4-b)thiophenediyl)) (PTB1) and PbS quantum dots. We employ ligand exchanges with various bidentate aliphatic thiol and carboxylic acid functionalized organic ligands including 1,2-ethanedithiol (EDT), 3-mercaptopropionic acid (MPA), and malonic acid (MA), in addition to inorganic halide ions using tetrabutylammonium iodide (TBAI). We use photoinduced absorption (PIA) spectroscopy to optically probe the generation and recombination of long-lived (μs-ms) photogenerated charged species in these blends. We also use transient photovoltage (TPV) and charge extraction (CE) techniques to determine the differences in carrier recombination rates and charge densities in the hybrid solar cells with different quantum dot ligands. We find that ligand exchanges yielding superior device performance correlate to higher long-lived charge generation yields and longer charge carrier recombination lifetimes under open-circuit conditions.

2.2 EXPERIMENTAL DETAILS

2.2.1 *Photoinduced Absorption (PIA) Spectroscopy*

Quasi-steady state and frequency-dependent PIA measurements were collected using standard lock-in techniques as we have described previously.[31, 47] The excitation source was a 447 nm LED (1030 mW Luxeon Rebel; LXML-PR02-A900), and was modulated at a frequency of 200 Hz with an Agilent 33120A arbitrary waveform generator through a home-built driver circuit.

The probe beam was a monochromated 100 W tungsten-halogen lamp, which was monitored with a dual-band Si/InGaAs photodetector (ThorLabs, DSD2) with spectral sensitivity from 500-1700 nm. For each wavelength measured, the fractional changes in probe beam transmission (ΔT) were detected by a Stanford Research Systems SR830 lock-in amplifier, and normalized to the total probe beam transmission (T) to yield the reported PIA signal as $\Delta T/T$. Each measured value of T was corrected for sample photoluminescence by recording data with the probe beam blocked. The phase of the lock-in was set using scattered pump light to make the measured signal entirely in the positive x-channel. Signal persisting longer than one duty cycle of the pump is represented in the quadrature (y-channel) signal that is opposite in sign to the x-channel (in-phase) signal. The data presented in the main text is the x-channel data scaled by the total signal magnitude $R = (x^2 + y^2)^{1/2}$ – in this manner the displayed intensities are proportional to the total signal R, but retain the phase (indicating absorption or bleach). The full PIA spectra can be found in Appendix A, **Figure A- 1**.

2.2.2 *PbS Quantum Dot Synthesis*

PbS QDs were synthesized using a modification of the protocol from Hines and Scholes.[48] The lead precursor was prepared in a three-neck flask with 450 mg (0.6 mmol) PbO, 14 g 1-octadecene (ODE), and 1.2 g (4 mmol) oleic acid. The mixture was stirred under vacuum at 100° C for at least 1 hr, turning the solution clear. The flask was placed under flowing nitrogen gas and the temperature was reduced to 90° C. Meanwhile, the sulfur precursor was prepared in a second 3-neck flask with 4 g ODE and 210 μL hexamethyldisilathiane (HMDS). The sulfur precursor was rapidly injected into the hot lead precursor, turning the solution black over the course of several seconds. Immediately following injection, the heating mantle was switched off, and the flask was left to slowly cool on the heating mantle. The product was isolated from the unreacted precursors by precipitation with acetone followed by centrifugation. The product was then cleaned in ambient air by dissolving the precipitated QDs in ~2 mL hexanes and precipitating once with acetone, and twice with methanol. The precipitated QDs were dried under flow of nitrogen gas.

A solution-based ligand treatment with butylamine was performed prior to blending the PbS QDs with the polymer in order to enhance device efficiencies, and is explained in Appendix A (see **Figure A- 2**). Butylamine treatment was achieved by dispersing the dry QDs in ~2 mL butylamine, followed by sonication for 30 min, then precipitation with isopropanol and centrifugation. The process was repeated once (for a total of two treatments). Finally, the QDs were dried under nitrogen flow and transferred into a nitrogen glove box and dispersed in anhydrous 1,2-dichlorobenzene. The QD solution was filtered through a 0.45 μm PTFE syringe filter prior to use. This treatment results in a broadening of the QD first exciton peak, accompanied by a small blue-shift of ~15 nm. We speculate that this observation indicates the partial removal of surface atoms from the QDs, possibly as Pb-oleate complexes to maintain charge balance. While the amount of butylamine on the QD surfaces following the exchange remains unclear, the FTIR spectra of the QD films show a decrease in the C-H stretching intensity of approximately 28% following butylamine treatment when comparted to as-synthesized QDs (result not shown), indicating only partial exchange of the native ligands.

2.2.3 *Preparation of TiO_2 Electrodes*

Zirconium-doped (5 at %) TiO_2 films of ~100 nm were prepared using a sol-gel method described by Liu *et al*.[45, 49] Briefly, 5 mL titanium (IV) *n*-butoxide and 0.35 mL zirconium (IV) *n*-butoxide (80% solution in butanol) were added to a mixture of 4 mL triethanolamine and 20 mL ethanol under magnetic stirring in air for 1 hr. A mixture of glacial acetic acid (5 mL) and deionized water (5 mL) were added dropwise to the flask and stirred for an additional 1 hr. The solution was filtered (0.45 μm pore size, PTFE) and stored in a vial. Prior to spin coating, ITO substrates were sonicated sequentially in 2% Micro-90 detergent, deionized water, acetone, then isopropanol for several minutes each. Films were spin-coated at 3000 RPM, then annealed on a hotplate at 500° C for 1 hr.

2.2.4 *Device Fabrication*

All device fabrication was performed in a nitrogen glove box to avoid oxygen and water contamination. PTB1 polymer (1-Material) was dissolved in 1,2-dichlorobenzene at a concentration of 10 mg/mL and stirred at 70° C until fully dissolved. The polymer/QD blend solution was made by mixing the PTB1 and PbS QD solutions in a 1:9 (w/w) ratio, such that the final concentration of the QDs was 62 mg/mL and the final concentration of polymer was 6.9 mg/mL. After stirring on heat for at least 1 hr, the blend solution was filtered and spin-coated on the ITO/TiO_2 substrates at 1000 RPM for 90 s. Post-deposition ligand exchange was performed based on previous reports,[9, 20-21] and verified by grazing angle attenuated total reflectance FTIR on QD-only films (Appendix A, **Figure A- 3**). Ligand exchange solutions were prepared by dissolving the ligands in anhydrous methanol at a concentration of 10 mM. The films were placed on the spincoater, and ~150 µL of the ligand exchange solution was pipetted on the film surface and allowed to sit for 60 s (or 15 s in the case of halide exchanges). The films were spun dry and the ligand treatment was repeated once and the sample was spun dry again. The film surface was then washed by pipetting pure methanol on the surface and spinning dry after 10 s. Finally, electrical contacts of MoO_x (10 mM) and Ag (100 nm) were applied by thermal evaporation under vacuum; MoO_x was typically deposited at a rate of 0.5 Å/s, and Ag at a rate of 1 Å/s. The PTB1/PbS QD films used for PIA studies were prepared under identical conditions on glass slides, without electrodes.

2.2.5 *Device Testing*

The device J-V characteristics were measured under simulated AM 1.5 solar illumination in a nitrogen glove box. The proper intensity was determined using a known photocurrent value for a calibrated Si photodiode masked with a 1.30 mm^2 aperture identical to those used for the devices. The dependence of J_{SC} on light intensity was determined by holding the device at J_{SC} (zero bias) under simulated solar illumination, and using a series of neutral density filters to vary the light intensity.

2.2.6 *Transient Photovoltage and Charge Extraction Measurements*

TPV and CE measurements were conducted using a home-built system modeled after detailed literature descriptions.[50-52] Completed devices were mounted in a home-built vacuum chamber under active vacuum (<20 mtorr). The devices were biased using constant white light illumination, provided by a white LED (Bridgbelux BXRA-56C9000-J) driven by a DC power supply, while the device was held at open circuit using a buffer with a 500 GΩ effective impedance. Voltage transients were generated with a blue LED (447 nm) pulsed at 2 Hz (4 µs width, 20 ns edge) with a home-built LED driver circuit and an Agilent 33210A 10 MHz function/arbitrary waveform generator, and measured by a Textronix TDS 2024B oscilloscope. CE measurements used a home-built driver to pulse the white LED while holding the device at open circuit to build carriers within the device. The white light was then turned off while simultaneously switching the device to short circuit, and the extracted current was shunted through a 511 Ω resistor. The oscilloscope was used to measure the corresponding voltage transient. The data was post-processed to convert the voltage transient to current volume using Ohm's law, the device thickness, and mask area. The charge carrier density (*n*) is then calculated via integration of the transients and dividing by the charge of an electron. The values obtained were then corrected for losses due to charge recombination. This was necessary because the bimolecular charge recombination lifetime is on the same timescale as the lifetime for charge extraction from the device at high light intensities (≥100 mW/cm^2) (Appendix A, **Figure A- 4**). The methods used for the corrections are found in Appendix A.

2.3 RESULTS AND DISCUSSION

We studied bulk heterojunction (BHJ) blends of PbS QDs with the low band gap polymer PTB1 blended in a 1:9 (w/w) ratio. **Figure 2-1**a shows the absorption spectra of PTB1 and PbS QDs (in tetrachloroethylene) and a PTB1/PbS QD blend film after post-deposition treatment with 3-mercaptopropionic acid (MPA). The first exciton transition of the PbS QDs is located at $\lambda = 900$ nm (~1.38 eV) in solution, corresponding to a QD size of roughly 3-4 nm.[53-54] The blend clearly shows contributions from absorption from both polymer and QD components. To study the influence of the QD ligands on the hybrid blends, we performed post-deposition ligand exchanges on films prepared under identical conditions with the series of ligands shown in **Figure 2-1**b. These treatments involved exposing the polymer/QD film to a methanol solution of the new ligand, resulting in exchange for the native QD ligands, as described in the Experimental section. The chemical structures of the ligands used in this study are shown in **Figure 2-1**b. In order to elucidate the effect of having both thiol and carboxylic acid functional groups on MPA molecules, we also tested a 1:1 mixture of EDT and MA. To ensure that the ligand treatments are not significantly interacting with the polymer component of the films, we measured the absorbance of neat polymer films before and after ligand treatment (Appendix A, **Figure A- 5**). We see no observable changes in steady-state absorption of the polymer post-ligand treatment, indicating that the polymer is chemically unaltered.

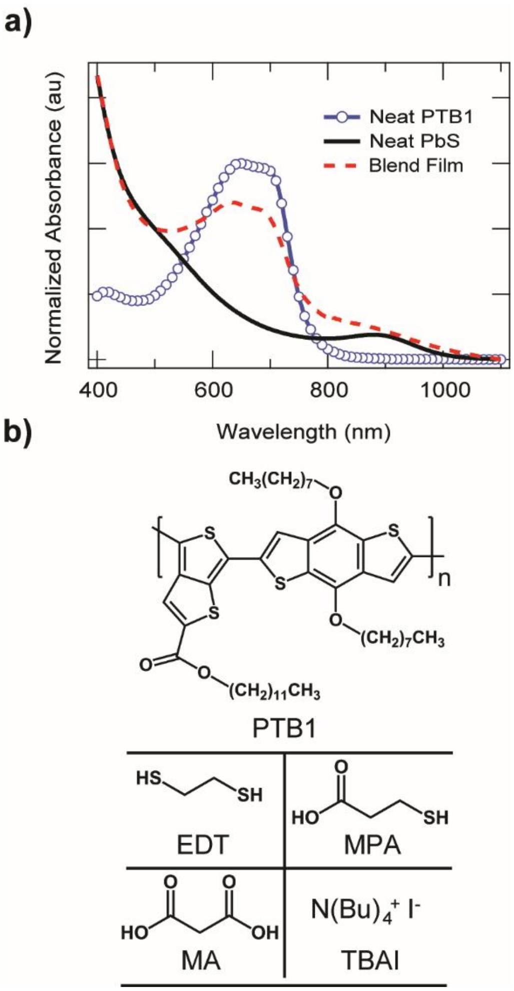

Figure 2-1. (a) Solution absorption spectra of PbS QDs (black, solid line) and PTB1 (blue, circle markers) in tetrachloroethylene, and a thin-film absorption spectrum of PTB1/PbS QD blend film (red, dashed line) after post-deposition ligand exchange with MPA. (b) Chemical structures of the PTB1 polymer and the ligands employed in this study.

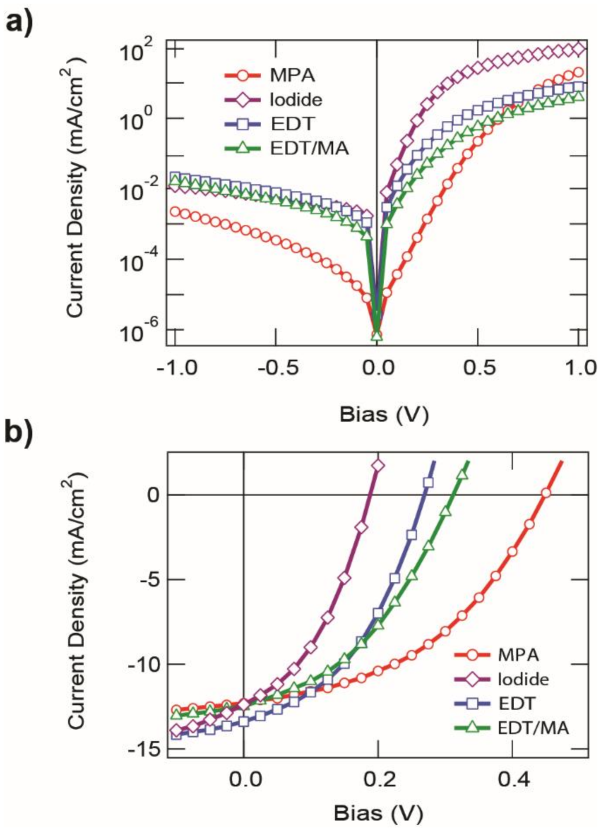

Figure 2-2. (a) Dark and (b) light *J-V* curves for PTB1/PbS QD devices subject to different ligand exchanges: MPA (red circles), TBAI (purple diamonds), EDT (blue squares), and a 1:1 mixture of EDT and MA (green triangles).

Table 2-1. Summary of Average Device Performance[a]

ligand	J_{SC}	V_{OC}	**FF (%)**	**PCE (%)**
MPA	11.02 ± 0.43	0.48 ± 0.01	47 ± 1	2.49 ± 0.10
EDT	13.07 ± 0.39	0.28 ± 0.02	44 ± 1	1.61 ± 0.10
EDT/MA	11.81 ± 0.38	0.32 ± 0.02	40 ± 1	1.51 ± 0.11
Iodide	12.00 ± 0.20	0.21 ± 0.01	40 ± 1	1.00 ± 0.05

[a] The values reported here are the averages and standard deviations of the mean of 16 different pixels (from 4 different devices) for each ligand type.

Figure 2-2 shows the *J-V* characteristics of the hybrid devices with different ligand treatments in the dark (a) and under AM 1.5 simulated solar illumination (b). The average device performance characteristics are given in **Table 2-1**. Importantly, changing the QD ligands primarily influences the device open-circuit voltage (V_{OC}) and fill factor (FF). Small enhancements in the average short-circuit photocurrent (J_{SC}) are observed for TBAI and EDT exchanges compared to MPA, which we attribute to enhanced light absorption in films using those ligands. We found that MPA treatment gave the highest power conversion efficiency (PCE) of the series, primarily due to the substantially higher V_{OC}'s of the MPA-treated devices. Ligand exchange with TBAI resulted in the lowest performance of the series with V_{OC} values less than half of that obtained from MPA devices, while EDT devices fall in between. The 1:1 mixture of EDT and MA results in similar performance to EDT-only devices, while exchange with malonic acid alone (not shown) results in poor diode performance and very little photocurrent generation (Appendix A, **Figure A- 6**). The low conductivity of MA-only devices in forward bias is consistent with the results of Zarghami *et al*. that show lower carrier mobilities in PbS QD films treated with oxalic acid, compared to those treated with monodentate carboxylic acid ligands of similar size.[55] We speculate that the poor electronic properties of PbS QDs treated with small dicarboxylic acid ligands may be predominantly from structural disorder of particle packing within the QD domains following ligand exchange, on the basis that carboxylate binding groups do not introduce electronic defects within the QD band gap, and the molecules are similar in size and structure to EDT and MPA. Our results differ from the case of all-PbS QD devices, in which incorporation of halide treatments have produced some of the highest efficiency devices to date.[28-29, 41, 56] Direct comparison of MPA and EDT treatments in depleted heterojunction devices show that MPA treatment offers a small improvement in V_{OC} and a substantial enhancement in photocurrent relative to EDT treatment.[57]

The strength of the QD-ligand surface dipole moment can shift the vacuum energy, and subsequently, the quantum dot valence band (VB) and conduction band (CB) energy levels by altering the electrostatic environment of electrons and holes transferred across the QD/ligand interface. The changes we observe in V_{OC} are at least partially consistent with the expectations based on the shift in QD band levels relative to the polymer levels due to differences in the net surface dipole of the QDs following ligand exchange (MPA < EDT < TBAI).[24] As the net surface dipole of the ligand increases, both valence band (VB) and conduction band (CB) energy levels of the QDs are pushed to deeper values,[24] leading to greater losses in V_{OC} as the energy difference between the donor polymer's ionization potential and the quantum dot CB edge is decreased (as shown in Appendix A, **Figure A- 7**). To examine the differences in device performance between different QD ligand exchanges in greater detail, we study the recombination characteristics of charge carriers in the devices under short circuit and open circuit conditions.

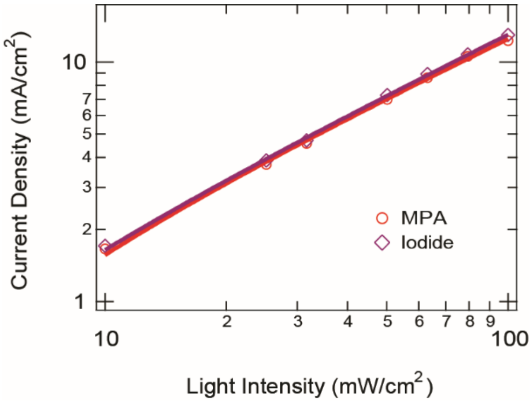

Figure 2-3. Dependence of short-circuit current density (J_{SC}) on incident light intensity for devices with MPA (red circles) and TBAI (purple squares) ligand exchanges.

Figure 2-3 shows the dependence of device J_{SC} as a function of incident light intensity for devices with the highest (MPA) and lowest (TBAI) PCE. We fit the data to a power law according to the relationship $J = I^{\alpha}$, where J is photocurrent and I is the incident light intensity. Charges at short circuit are rapidly swept out of the device, and the parameter $\alpha = 1$ when all carriers are swept out prior to recombination.[58] Values of α below unity indicate non-first order recombination processes occur at short circuit, which can result for a variety of reasons including bimolecular recombination, space-charge effects, or differences in mobility between the electrons and holes.[58] We observe very similar light intensity dependence for the J_{SC} of all the ligands, with $\alpha \sim 0.9$ for all devices (see **Table A- 1** in Appendix A). The data comparing all ligand treatments is shown without fits in Appendix A, **Figure A- 8**. These data indicate that the recombination dynamics at short-circuit for the hybrid devices are independent of the ligand identity, and only weakly dependent on light intensity.

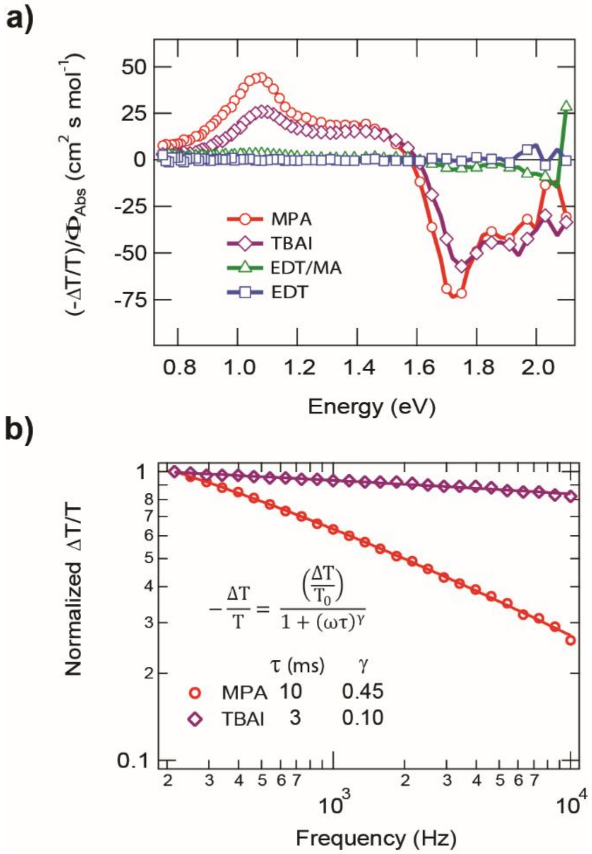

Figure 2-4. a) Quasi-steady state PIA spectra of PTB1/PbS QD films treated with MPA (red circles), TBAI (purple diamonds), EDT (blue squares), and a (1:1) EDT/MA mixture (green triangles). b) Pump modulation frequency dependence of the differential transmission (-ΔT/T) monitored at the 1.1 eV polaron peak. Decay parameters (τ and γ) were found from dispersive fits according to the inset model.

We use photoinduced absorption (PIA) spectroscopy to study the dynamics of long-lived (μs-ms) charges in the polymer/QD blends. Since there are no electrical contacts to the films, we expect these PIA measurements to probe intrinsic recombination dynamics in bulk of the film at V_{OC}. **Figure 2-4**a shows the PIA spectra of PTB1/PbS films treated with the series of different ligands shown in **Figure 2-1**b. The spectra have been scaled by the absorbed photon flux at the excitation wavelength (Φ_{Abs}/mol cm^{-2} s^{-1}), allowing comparison of long-lived polaron yields based on PIA signal magnitudes. The spectra show the ground-state bleach of the polymer from 2.25-1.6 eV. The positive absorption feature located at ~1.1 eV is attributed to polarons on the PTB1 chains, as described previously for this system.[37] We observe long-lived polaron formation only in blends treated with MPA and TBAI. The polaron yield (corrected signal magnitude at the polaron peak) for MPA treatment is approximately twice the yield measured for TBAI treatment. No signal is observed for blends treated with EDT or the EDT/MA mixture. Interestingly, films treated only with MA do show formation of polarons (see Appendix A **Figure A- 1**), while the EDT/MA mixture shows no PIA signal, consistent with EDT-only treatment.

Figure 2-4b shows the dependence of the PIA signal at the polaron peak (1.1 eV) on the pump modulation frequency. The faster roll-off characteristics of the MPA blend indicates longer average polaron lifetimes compared to the TBAI blend. These data were fit with a dispersive lifetime model to determine the kinetics of the measured species.[59] The lifetime parameters obtained from the fits were $\tau \approx 10$ ms and $\tau \approx 3$ ms for MPA and TBAI treatment, respectively. Taken together, the PIA data shows that blends treated with MPA exhibit both higher charge generation yields and longer recombination lifetimes than blends treated with TBAI. These trends in carrier lifetime help explain the higher V_{OC} and FF of the devices treated with MPA. Since the maximum V_{OC} is limited by the degree of quasi-Fermi level splitting obtained under illumination, longer free carrier lifetimes allow greater charge populations to accumulate, leading to higher obtainable open circuit voltages.[60]

To further investigate the differences in charge recombination in operational solar cells under open-circuit conditions, we employ transient photovoltage (TPV) and charge extraction (CE) techniques. Briefly, the device is held at open-circuit while biased using constant white light illumination which creates a background carrier density, n. A weak perturbation light pulse is used to create a small excess of charge carriers to the significantly larger background level. This is measured as a small perturbation to the voltage output, and can be fit with a single exponential decay function to extract the small perturbation (pseudo-first-order) carrier decay lifetime $\tau_{\Delta n}$.[61] CE is a complementary technique that can be used to measure the charge carrier densities (n) at light intensities matching those used in the TPV experiment.[50-51]

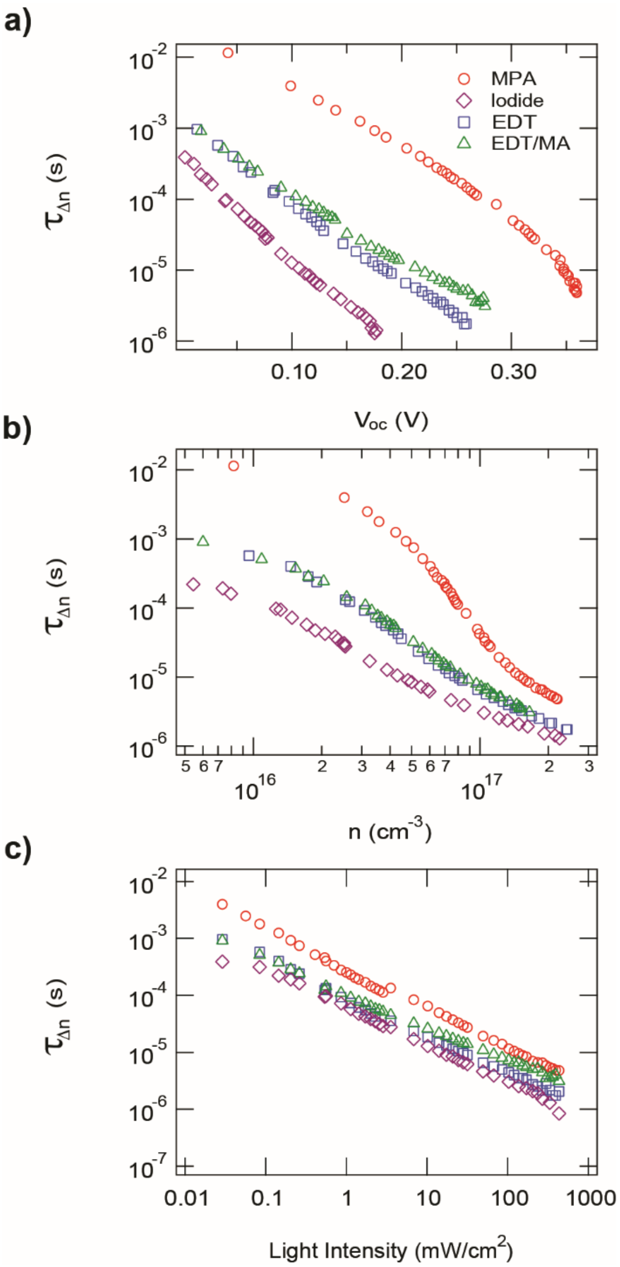

Figure 2-5. Carrier recombination lifetime ($\tau_{\Delta n}$) as a function of (a) V_{OC} and (b) charge carrier density (*n*) and (c) incident light intensity for PTB1/PbS QD solar cells treated with MPA (red circles), TBAI (purple diamonds), EDT (blue squares), and a (1:1) EDT/MA mixture (green triangles).

Figure 2-5a shows the charge carrier decay lifetimes as a function of V_{OC} for devices treated with the series of ligands from **Figure 2-1**b. We observe that at each value of V_{OC}, MPA exhibits the longest lifetimes, followed by EDT, then TBAI. The EDT/MA treatment, again, had very similar characteristics to the EDT-only device. We observe similar characteristics for the measured recombination lifetimes as a function of charge carrier density (**Figure 2-5**b). Importantly, this result shows that for matched charge densities, the recombination lifetimes observed for MPA treatment are one-to-two orders of magnitude longer than those obtained for EDT and TBAI in devices at open circuit.

Notably, the trends in recombination lifetime ligand treatments obtained from transient photovoltage data in **Figure 2-5** are in good agreement to those obtained by fitting the photoinduced absorption frequency-dependence data in **Figure 2-4**b. Both trends are therefore self-consistent in explaining the higher V_{OC} and FF of the MPA treated devices as arising from reduced non-geminate recombination in these films. We note that a previous study from Jeong and coworkers reports longer excited state lifetimes of PbS QDs exchanged with EDT ($\tau = 93$ μs) compared to MPA ($\tau = 31$ μs).[57] However, that work measured the decay rate of excited carriers in PbS QD films from shallow trap states to the ground state using time-resolved infrared (TRIR) spectroscopy. In contrast, here we are measuring bimolecular recombination lifetimes of free carriers at interfacial sites between donor and acceptor species where MPA exchange yields longer lifetimes than EDT exchange. We also note that the trend in carrier recombination rates is opposite that of the driving force for recombination (*i.e.* MPA treatment has the highest driving force for recombination but the longest carrier lifetimes). In the absence of other changes, this might suggest that recombination in this system is a Marcus inverted process in which the recombination rate is reduced with increasing driving force. However, we speculate that differences in trap state density and mobility between the different ligands may play the dominant role in the recombination of carriers we measure here.

As expected the differences in TPV lifetime as a function of V_{OC} or *n* are larger than the differences in average polaron recombination lifetimes determined spectroscopically using PIA, which differ by a factor of about three. Because carrier recombination rates depend on light intensity at V_{OC}, and PIA data was collected for all samples under matching pump intensity, we accordingly compare the TPV lifetimes as a function of background white light intensity as shown in **Figure 2-5**c. This demonstrates that the differences in recombination rates between ligand exchanges obtained via TPV are similar in scale to the average polaron decay rates measured in PIA. The remaining differences between PIA and TPV experiments may be the result of differences in interfacial recombination, or internal field and carrier profiles in the completed devices compared to the films used in PIA.[52]

2.4 CONCLUSIONS

We compared the effects of a variety of PbS surface treatments including MPA, EDT, MA, and TBAI on the performance of PbS/PTB1 solar cells. We obtained the best overall device efficiencies using MPA as a ligand and found that ligand chemical identity influences the photovoltaic performance of devices primarily through V_{OC} and fill factor. The recombination dynamics under short circuit conditions show only a small deviation from first-order kinetics that are independent of ligand identity. However, under open-circuit conditions, both photoinduced absorption measurements on blended films and transient photovoltage measurements on devices show that ligand treatments resulting in lower V_{OC} values exhibit faster carrier recombination rates, while the MPA treatment gave the longest carrier lifetimes, thus explaining the higher V_{OC} and FF of the MPA-treated devices. This work highlights the opportunity of using QD ligand selection to tailor recombination kinetics at the donor/acceptor interface in hybrid polymer/QD solar cells.

Chapter 3. HOLE TRANSFER FROM LOW BAND GAP QUANTUM DOTS TO CONJUGATED POLYMERS IN ORGANIC/INORGANIC HYBRID PHOTOVOLTAICS

Adam E. Colbert, Eric M. Janke, Stephen T. Hsieh, Selvam Subramaniyan, Cody W. Schlenker, Samson A. Jenekhe, David S. Ginger

3.1 INTRODUCTION

Blends of conjugated polymers with inorganic nanoparticles are promising as solution processable materials both for large area, low cost solar cells,[12-13, 15, 17, 19-21, 31-32, 62-63] and also for high efficiency infrared photodetectors and image sensors.[5, 39, 64] However, the highest efficiencies of organic/inorganic hybrid photodiodes[13, 19-21, 32, 63, 65] have tended to lag behind those of all-organic (polymer/fullerene) bulk heterojunction diodes.[11, 66-68] Despite this performance gap, inorganic hybrids have several potential advantages, particularly for infrared light harvesting at precisely tailored energies, as might be desirable in a tandem solar cell, or an infrared sensor. Understanding the mechanistic details of how these blends convert light into current is thus an important step towards rationally engineering better performing devices.

Generally, polymer/quantum dot composites are believed to operate as hybrid bulk heterojunctions.[12, 17, 19, 32] In a hybrid bulk heterojunction, light absorption by the organic host creates neutral excitons which are dissociated to free charges by electron transfer to the inorganic nanoparticles. Direct evidence for photoinduced electron transfer from the polymer to the quantum dots following excitation of the polymer host (or both the polymer and quantum dots) has been obtained in a number of polymer/quantum dot blends using both steady-state[17, 31-32, 59] and ultrafast[19, 39, 64, 69-71] spectroscopy experiments.

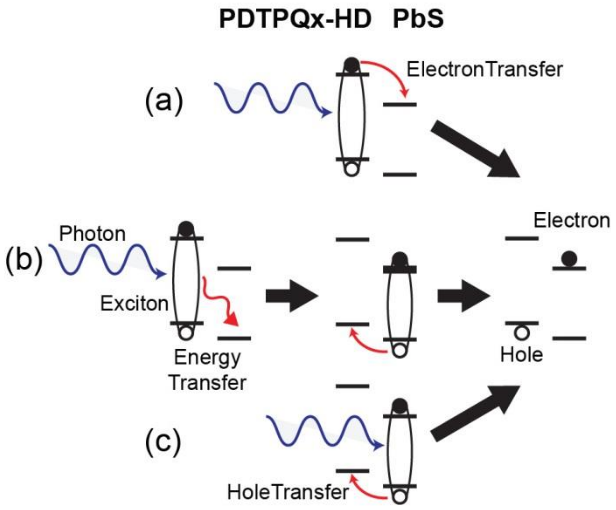

Figure 3-1. Possible charge separation pathways in semiconducting polymer/quantum dot blends. (a) photoexcitation of the polymer followed by electron transfer to the quantum dot. (b) photoexcitation of the polymer followed by energy transfer of the exciton to the quantum dot, and subsequent hole transfer to the polymer. (c) photoexcitation of the quantum dot followed by hole transfer to the polymer.

However, other pathways for photocurrent generation exist (**Figure 3-1**).[12] When the bandgap of the quantum dots is smaller than the bandgap of the organic host, photocurrent could also arise due to light absorption by the polymer followed by energy transfer to the low-bandgap quantum dots. Likewise, the quantum dots could directly absorb the incident light. Both processes produce an exciton on the quantum dot. At that point, photocurrent could arise either via hole transfer from the quantum dot to the polymer (process b and c in **Figure 3-1**), or alternatively via direct separation of the electron-hole pair in the quantum dot phase due to band bending near the contacts (an internal Schottky diode). Indeed, quantum dot Schottky diode devices can produce large photocurrents even in the absence of any polymer.[27, 72-75]

The possibility for hole transfer from the quantum dots to the polymer (process c in **Figure 3-1**) has been recognized since the earliest reports of photovoltaic action in polymer/quantum dot blends.[12, 31] Although photoluminescence quenching has been reported in polymer/quantum dot blends with low band gap quantum dots,[39, 64-65] there has been little evidence to confirm that hole transfer from the quantum dots to the polymer host actually produces long-lived charges in binary blends. Here, we provide direct spectroscopic evidence that hole transfer produces long-lived charges in a hybrid polymer/quantum dot bulk heterojunction composite. Furthermore, we quantify the relative hole polaron yields following direct excitation of the polymer and quantum dots in the solid blend films.

3.2 EXPERIMENTAL DETAILS

3.2.1 *PbS Quantum Dot Synthesis and Halide Treatment*

Colloidal PbS QDs were synthesized using a modified procedure described by Hines and Scholes.[48] Surface passivation by a partial oleate-to-iodide ligand exchange was performed in-situ based on the work of Ning et al.[56] The lead precursor was prepared by mixing PbO (0.446 g, 2.00 mmol), oleic acid (1.6 g, 5.66 mmol), and 1-octadecene (ODE) (14 g) in a three-neck flask and stirring under vacuum at 105° C for at least 1 hr. After the solution turned clear, the flask was placed under nitrogen flow and the temperature was increased to 165° C. Meanwhile, iodide and sulfur precursors were prepared in separate three-neck flasks. For the iodide precursor, oleylamine (0.8 g, 3 mmol) and tetrabutylammonium iodide (TBAI) (200 mg, 0.55 mmol) were added to a 25 ml flask 3-neck flask and degassed under vacuum. While stirring under vacuum, the iodide precursor was heated to 200° C for 1 hr. Subsequently, the temperature was reduced to 50° C, vacuum was ceased and the flask remained under nitrogen flow. The sulfur precursor was prepared in a separate three-neck flask by addition of 210 μL (1 mmol) Hexamethyldisilathiane (HMDS) to 4 g of ODE under nitrogen gas flow. The sulfur precursor was rapidly injected into the hot lead precursor solution. Upon injection, heat to the reaction flask was immediately switched off and the mixture was left on the heating mantle to slowly cool.

Once the temperature of the reaction solution reached 70° C, 0.75 mL of the contents of the iodide precursor flask was injected into the PbS colloid flask and stirred under flow of nitrogen for 20 min. The quantum dot product was isolated from the unreacted precursors by precipitation with acetone followed by centrifugation. The product was cleaned in ambient air by dissolving the precipitate in a minimal volume of hexanes and precipitating once with acetone and twice with methanol. The final product was dried under nitrogen and transferred to a glovebox where it was dissolved in anhydrous chlorobenzene.

3.2.2 *ZnO Nanocrystal Synthesis*

Colloidal ZnO nanocrystals were prepared in ambient atmosphere using an adaptation of procedures described elsewhere.[70, 76-77] Briefly, zinc acetate dihydrate (5.25 g, 24 mmol) was dissolved in 200 ml methanol by stirring at 60° C and subsequently reacted via dropwise addition of 100 mL of 0.4 M KOH in methanol. The mixture was stirred under mild refluxing conditions for 2 hr. The resulting opaque white colloid was isolated from unreacted precursors by centrifugation at 1200 rpm. The isolated nanocrystals were cleaned 3 times by addition of 10 mL methanol, agitation by vortexing, and centrifugation, discarding the supernatant between cycles. Finally, the ZnO nanocrystals were dispersed in chloroform at a concentration of ~80 mg/mL.

3.2.3 *Device and PIA Sample Fabrication*

Pre-etched 1.5 cm^2 substrates of indium tin oxide (ITO) coated were cleaned by sonication in acetone followed by isopropanol for 30 min each. ITO substrates were then cleaned by air plasma treatment for 10 minutes. ZnO was immediately spin-cast from a chloroform solution at 2500 rpm to give a ~65 nm coating of ZnO nanocrystals (as measured by profilometry). Coated substrates were then annealed at 250° C for 30 minutes in air, then cooled to room temperature. All subsequent sample preparation steps were performed in a nitrogen glovebox. A 20 mg/mL solution of PDTPQx-HD was prepared in anhydrous chlorobenzene and stirred at 50° C for at least 4 hr. A blend solution was prepared by mixing the PbS and PDTPQx-HD solutions in a 1:9 (w/w) ratio, and stirring at 50° C for at least 4 hr. PDTPQx-HD/PbS active layers were then spin-cast on ZnO coated ITO by a 2 seconds at 1200 rpm followed by 1 minute at 1800 rpm. PDTPQx-HD/PCBM blends were prepared in a similar manner by mixing the PDTPQx-HD solution with a 40 mg/mL solution of $PC_{61}BM$ in chlorobenzene in a 1:1 (w/w) ratio. For PIA samples, films were spin cast under the same conditions onto glass microscope slides. Spin-cast films were treated with 3-mercaptopropionic (MPA) to remove insulating oleate ligands and passivate the surface according to a procedure adapted from the literature.[25, 41] Films were treated with a 1 mmol solution of MPA in anhydrous methanol three times by coating the film surface with the solution, waiting for 1 minute, then blowing the film dry with a stream of nitrogen. The films were subsequently washed with anhydrous methanol and blown dry three times to remove residual quantum dot ligand. Photovoltaic device back contacts of MoO_3 (10 nm)/Ag (100 nm) were and were deposited by consecutive thermal evaporations from a base pressure of less than 5×10^{-7} torr. Individual pixels were defined by a shadow mask.

3.2.4 *Photovoltaic Device Measurements*

Photocurrent spectra were obtained with a monochromated tungsten-halogen lamp and measured with a Keithley 2400 source measure unit. External quantum efficiency (EQE) values were calculated using calibrated silicon (OSI optoelectronics) and indium gallium arsenide (Thorlabs) photodiodes. The calibrated photodiodes and the device pixels were masked with identical 1.22 mm^2 active areas. The devices were held under active vacuum during device testing.

3.2.5 *Photoinduced Absorption Measurements*

PIA and frequency-dependence measurements were acquired using standard lock-in techniques detailed elsewhere.[31, 47] The 2.77 eV (447 nm) excitation source was a light-emitting diode (LED; Luxeon Rebel, 700 mW, LXML-PR01-0425) equipped with a 550 nm long pass filter to block pump light from entering the detector. The 1.95 eV (635 nm) pump was an LED (Luxeon Rebel, 700 mW, LXM2-PD01-0040) equipped with a 700 nm long pass filter. Both LEDs were powered with a home-built driver circuit. The LEDs were modulated by an Agilent 33120A arbitrary waveform generator. The 1.27 eV (975 nm) excitation source was a 1000 mW laser diode (ThorLabs L975P1WJ), modulated with an optical chopper (Stanford Research Systems SR540). Quasi-steady-state measurements were conducted with a pump modulation frequency of 200 Hz. The probe beam was a monochromated 100 W tungsten halogen lamp and was monitored with with a Si/InGaAs dual-band photodetector (ThorLabs, DSD2) with sensitivity ranging from 500-1700 nm in the case of quasi-steady-state measurements, or an amplified Si photodiode (ThorLabs PDA36A) with sensitivity up to 1100 nm in the case of frequency-dependence measurements. At each measured probe energy, fractional changes in probe beam transmission (ΔT) were detected with a Stanford Research Systems SR830 lock-in amplifier which were normalized to the probe beam transmission (T), and corrected for sample photoluminescence by recording data with the probe beam blocked. Values are reported as normalized negative differential transmission ($-\Delta T/T$). The phase of the lock-in was set using reflected pump light such that the signal was entirely in the positive X-channel (in-phase). The Y-channel (quadrature) detector is 90° phase lagged from the X-channel. Samples were held under active vacuum during PIA measurements.

3.3 RESULTS AND DISCUSSION

As a model system, we study blends of PbS quantum dots with the host polymer poly(2,3-bis(2-(hexyldecyl)-quinoxaline-5,8-diyl-*alt*-N-(2-hexyldecyl)-dithieno[3,2-b:2′,3′-d]pyrrole) (PDTPQx-HD). This blend has previously been shown to form a bulk heterojunction with PbS quantum dots.[17, 32] To facilitate charge transfer between the polymer electron donor and the quantum dot electron acceptors, we treated the quantum dot surfaces with a hybrid passivation scheme adapted from recent works by the Sargent group for fabricating PbS colloidal quantum dot photovoltaics.[41, 56] The quantum dots were first solution-phase halide treated with tetrabutylammonium iodide (TBAI). A PDTPQx-HD/PbS (1:9 w/w) blend was then spin-cast from anhydrous chlorobenzene, and the films were subsequently treated with a 1 mM solution of 3-mercaptopropionic acid (MPA) solution in anhydrous methanol as detailed in the Appendix B. The hole transfer mechanism was investigated using quasi-steady-state photoinduced absorption (PIA) spectroscopy.[17, 31-32, 47, 59] Films for PIA experiments were prepared on glass substrates and fabricated under the same conditions as the photovoltaic devices.

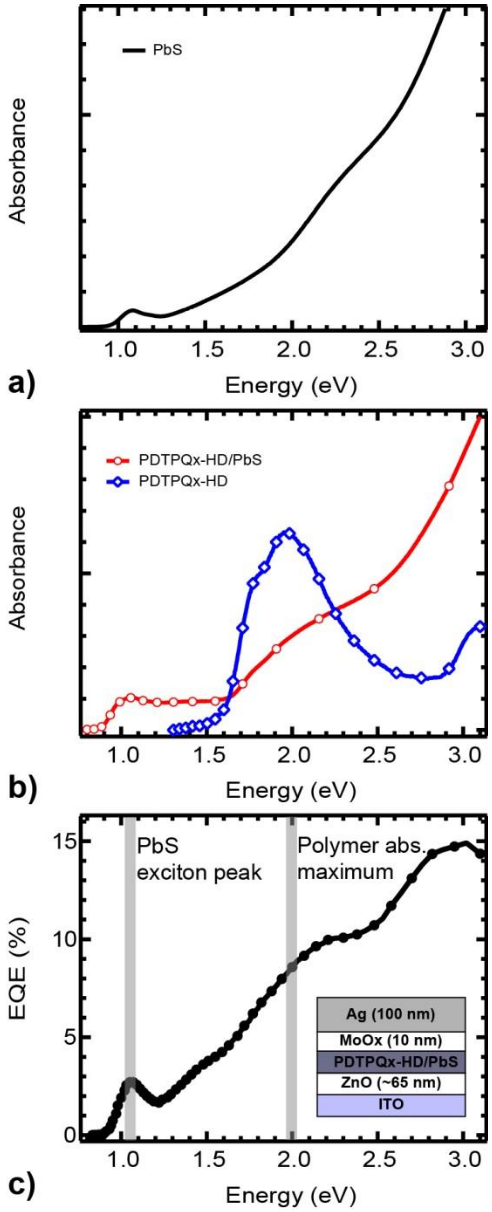

Figure 3-2. (a) Absorbance spectra of PbS in tetrachloroethylene, (b) Pristine PDTPQx-HD thin film (blue diamonds), and PDTPQx-HD/PbS-hybrid passivated thin film (red circles). (c) EQE spectrum for a PDTPQx-HD/PbS-hybrid passivated bulk heterojunction blend device. The gray regions highlight the polymer absorption maximum (~1.94 eV) and the PbS quantum dot exciton peak (~1.05 eV). The inset shows the device structure.

Figure 3-2a and 3-2b compare the absorbance spectra of PbS solutions and pristine PDTPQx-HD films with the polymer/PbS blend film used for photovoltaic device and PIA measurements. The PbS quantum dots used in these experiments have a quantum confined exciton absorption (E_g = 1.07 eV, 4 nm diameter), while the pristine PDTPQx-HD film begins absorbing at ~1.55 eV, and has an absorption maximum at 1.94 eV. As expected, the first exciton absorption peak of the PbS quantum dots in the solid blend film is slightly redshifted (~0.2 eV) from the exciton peak in solution due to dielectric and close-packing effects of the quantum dots in films, and the post-deposition ligand treatment. The blend also shows a pronounced shoulder at ~2.0 eV, corresponding to the position of the PDTPQx-HD absorption peak.

Figure 3-2c shows the external quantum efficiency (EQE) spectrum from a PDTPQx-HD/PbS photovoltaic device with the structure (ITO/ZnO (65 nm)/active layer/MoO_x (10 nm)/Ag (100nm)) with a peak EQE reaching 15%. The spectrum shows contributions to the device photocurrent from both polymer and quantum dot species with a clear quantum dot exciton peak at ~1.05 eV, and a shoulder around ~2.0 eV due to the polymer absorption peak. We interpret this spectrum as evidence that the device functions as a bulk heterojunction in which photogenerated excitons dissociate via charge transfer at the donor/acceptor interface. The photocurrent observed at energies below the polymer band gap (~1.7 eV) arises only from light absorbed by the PbS quantum dots. The source of this photocurrent could arise from either hole transfer from the QDs to the polymer, or from direct exciton dissociation in the QD percolation networks (acting as Schottky diode pathways). To determine whether the hole transfer mechanism is possible in these blends, we used photoinduced absorption to determine whether selective excitation of the quantum dots leads to the formation of positively charged polarons on the polymer.

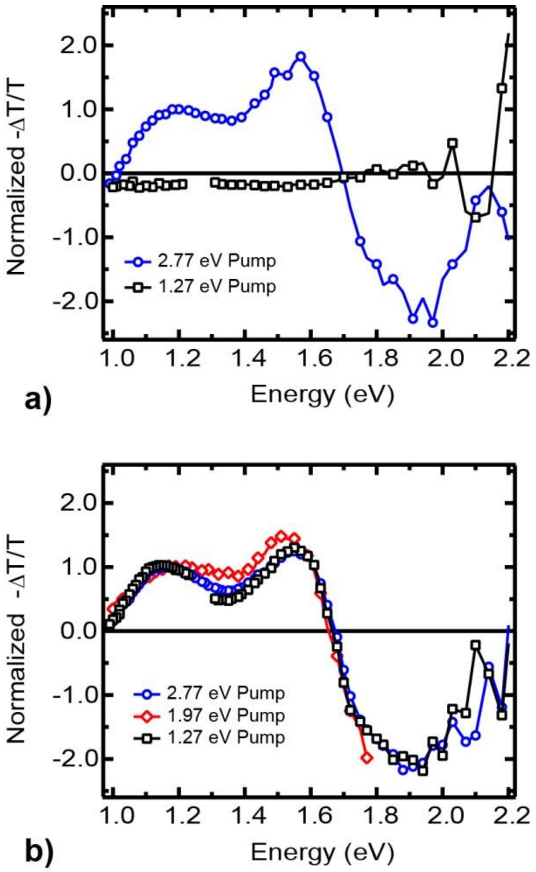

Figure 3-3. X-channel (in-phase) photoinduced absorption spectra normalized to the positive polaron transition peak at 1.18 eV. (a) shows the PIA spectra for PDTPQx-HD/PCBM (control) using excitation at 2.77 eV (blue circles), and 1.27 eV excitation (black squares). (b) MPA-treated PDTPQx-HD/PbS excited with 2.77 eV (blue circles), 1.97 eV (red diamonds), 1.27 eV (black squares).

Figure 3-3a compares PIA spectra of a reference PDTPQx-HD/ [6,6]-phenyl C60 butyric acid methyl ester ($PC_{61}BM$) blend under 2.77 eV (blue circles) and 1.27 eV (black squares) photoexcitation. Sample excitation with the 2.77 eV pump shows a characteristic HOMO-LUMO bleach feature between 1.2-1.6 eV, and a broad induced absorption feature from 0.9-1.6 eV, in accordance with previously reported data.[17, 32] We attribute these features to the formation of long-lived positive charge carriers (polarons) on the polymer chains resulting from charge transfer between electron donor and acceptor species. Importantly, we note that the 1.27 eV pump does not produce any detectable PIA signal, since neither PDTPQx-HD nor PCBM absorb at 1.27 eV in the ground state (Appendix B, **Figure B- 2**). The band at 1.6 eV has previously been assigned as an electroabsorption (EA) feature,[17] although a detailed understanding its physical origins is beyond the scope of this work. The pump modulation-dependence of the EA and polaron features for PDTPQx-HD/PCBM are shown in Appendix B (**Figure B- 3**).

Figure 3-3b compares PIA spectra of a hybrid passivated PDTPQx-HD/PbS blend under 2.77 eV (blue circles), 1.97 eV (red diamonds) and 1.27 eV (black squares) photoexcitation (Un-normalized spectra are found in Appendix B, **Figure B- 4**). Since the MPA ligand treatment does not affect the polymer (section B5 in Appendix B), we attribute the observed polaron formation to charge transfer between polymer and quantum dot species. The 2.77 eV and 1.97 eV pumps excite both the PDTPQx-HD polymer and the PbS quantum dots. The observed polaron spectra could thus arise from any of the pathways shown in **Figure 3-1**. However, the 1.27 eV pump excites only the PbS quantum dots. We observe a polaron spectrum on the polymer following this selective photoexcitation of the PbS that is virtually identical to that obtained by photoexciting the PDTPQx-HD in the polymer/fullerene blend. This result demonstrates that pathway c in **Figure 3-1** is possible, and provides direct spectroscopic evidence of hole transfer from quantum dot to polymer in a hybrid bulk heterojunction composite. The ground-state bleach of the quantum dot first excitonic transition at the optical band gap (E_g = 1.07 eV) overlaps the polaron shoulder, and is hidden by the polymer polaron absorption (section B6 in Appendix B).

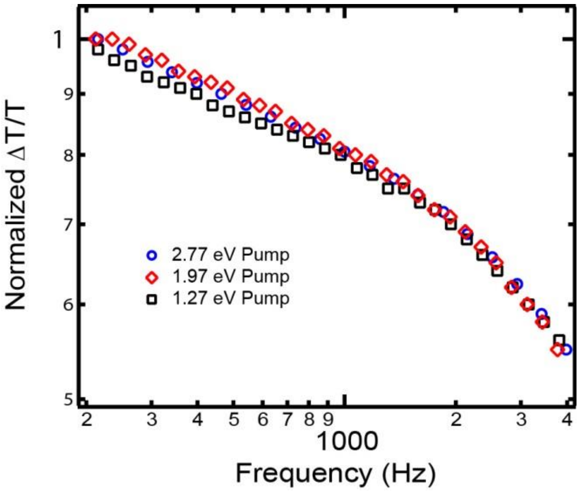

Figure 3-4. PIA pump modulation frequency dependence of the PDTPQx-HD/PbS sample from Figure 3-3b, measured at the polaron transition peak (1.18 eV) with 2.77 eV (blue circles), 1.97 eV (red diamonds), and 1.27 eV (black squares) excitation.

Next, we examine the recombination kinetics of long-lived polarons formed in PDTPQx-HD/PbS blends by measuring the PIA signal dependence on pump modulation frequency. **Figure 3-4** compares the pump modulation dependence of the PIA signal from **Figure 3-3**a at all 3 pump energies. The probe energy was fixed at 1.18 eV to monitor the pump frequency-dependence of the polaron transition. **Figure 3-4** shows that the modulation dependence, and hence the polaron lifetime distribution, is virtually identical regardless of excitation wavelength. This result indicates that, at least on microsecond-to-millisecond timescales, the distribution of occupied polaron sites on the polymer is relatively insensitive to the formation history (excitation of the polymer, or excitation of the quantum dot phase). Fitting a dispersive lifetime model,[10,20] the frequency dependence of the PIA signals at each excitation wavelength gave similar lifetime (τ) distributions of $\tau \approx 0.25$ ms and dispersion parameter (γ) of $\gamma \approx 0.67$ (see Appendix B, **Figure B- 7**).

Finally, we note that the data in **Figure 3-2**, **Figure 3-3**, and **Figure 3-4** allow us to estimate the ratio of long-lived charge carriers generated following excitation of the polymer or quantum dots. To do so, we make the assumption that the polaron yield in each species is independent of excitation wavelength (in other words, that hole transfer from the quantum dots to the polymer is the same if the quantum dots are excited at 1.27 eV, 1.97 eV, or 2.77 eV), and that the total polaron signal is thus a linear superposition of charge generated by charge transfer from photoexcited PbS to the polymer, and from photoexcited polymer to the PbS. Knowing the (unnormalized) PIA signal magnitudes, the pump fluences, and absorbance spectrum of the film, we can then calculate the relative polaron yields of the polymer and quantum dot components at matched excitation densities (see section B8 of Appendix B). Doing so, we estimate that ~2.5X as many long-lived polymer polarons are produced per photon absorbed by PDTPQx-HD compared with photons absorbed by the PbS quantum dots (under the assumption that hot electron transfer processes are negligible). This result is qualitatively consistent with our previous observation that the internal quantum efficiency (collected photocurrent per photon absorbed) in blends of this polymer with PbS quantum dots is higher for photons absorbed in the visible rather than in the infrared.[32] Various mechanisms could be invoked to explain the relative difference in polaron yields following excitation of the quantum dots or excitation of the polymer. One explanation could be the larger driving force for electron transfer from the photoexcited polymer to the quantum dots than for holes from the photoexcited quantum dot to the polymer (-0.52 eV vs. -0.27 eV) (see Appendix B

Figure B- 10). Another possibility is that the hole transfer yield depends on excitation wavelength. At higher excitation energies, the relative yield of hole transfer might go up due to hot holes transferring from the PbS to the polymer (which would appear as higher yield of polymer-to-PbS electron transfer in our calculation).

3.4 CONCLUSIONS

In summary, we have used photoinduced absorption spectroscopy to observe hole transfer in a hybrid infrared-sensitive polymer/quantum dot bulk heterojunction blend. We have obtained direct spectroscopic evidence of long-lived hole transfer from the quantum dot species to the organic polymer host. In the future, we anticipate that studies of hole transfer from quantum dots to polymer hosts may help us to better understand the importance of driving force and hole transfer in polymer/fullerene solar cells as well.[78-79] Interestingly, the relative yield of long-lived polarons following IR photoexcitation of the quantum dots seems to be lower than when the polymer is excited directly in the visible. This observation may help explain the somewhat lower internal quantum efficiencies that these blend exhibits when excited in the infrared rather than the visible, and could point the way towards improved efficiencies. At present, the reason for this discrepancy remains an open question for future study, although it is possible that both driving force and hot electron transfer processes[80-81] could play a role.

Chapter 4. SUBPICOSECOND PHOTON-ENERGY-DEPENDENT HOLE TRANSFER FROM PBS QUANTUM DOTS TO CONJUGATED POLYMERS

Adam E. Colbert, Erin Jedlicka, Wenbi Wu, and David S. Ginger

4.1 INTRODUCTION

In addition to potential applications in solution-processable light-emitting diodes[82-84] and solar cells,[14, 18, 85] quantum dot/conjugated polymer composites represent an interesting model system for studying the effects of driving force,[37, 86] morphology,[87-88] and surface chemistry[18, 21-22, 40] on charge transfer and recombination processes in the condensed phase. For instance, in the context of organic solar cells, photoexcitation of an organic material generates bound excitons, which has motivated the use of heterojunctions to separate electrons and holes at donor/acceptor interfaces. The dynamics governing the efficiency of free carrier generation in the resulting bulk heterojunction (BHJ) solar cells has been the subject of extensive research in both polymer/fullerene[89-92] and polymer/quantum dot blends.[34-35, 86, 93] Considerable interest centers on the degree to which excess energy associated with nonthermalized "hot" excited states influence free carrier generation. Some studies have highlighted the role that above-gap excitation plays in the formation of free carriers.[91, 94-96] However, other studies show that the internal quantum efficiency (IQE) of devices using various polymer/fullerene blends is relatively constant,[79, 97-98] even out to the low energy charge transfer (CT) state,[92] suggesting that the generation of hot carriers is not necessary for efficient charge separation.

In the case of colloidal semiconductor quantum dots (QDs), hot carrier dynamics are of interest for their importance in multi-exciton generation (MEG)[99-100] and hot carrier extraction.[101-103] The well-separated energy levels of highly confined QDs may serve to reduce carrier relaxation rates that occur through phonon emission.[104] Despite the predicted "phonon bottleneck," carrier relaxation times for lead chalcogenide (PbS and PbSe) QDs have been reported within the range of 0.2-6 ps.[102, 105-106] Some studies have attributed the fast intraband relaxation observed in QDs to the dissipation of energy through surface ligand vibrational modes.[106-107] These cooling rates can also result from Auger-assisted relaxation, whereby the excess energy of the electron is transferred to the hole, followed by rapid relaxation via phonon emission due to the larger hole density of states.[108-109] However, PbS and PbSe QDs have demonstrated efficient ultrafast (<100 fs) electron transfer to TiO_2 films that can compete with carrier relaxation times.[101-103]

Relative to bulk heterojunctions incorporating organic fullerene molecules as the acceptor material, less is understood about the process of charge generation in polymer/quantum dot blends. Recent studies have demonstrated ultrafast charge transfer in polymer/QD systems through selective excitation of either the donor polymer[86] or the QD component.[18] However, the role of hot carriers and energetic driving force for charge transfer in QD/organic heterojunctions has been less studied.[34, 37, 110] Previous work from our group demonstrated the IQE in a polymer/PbS QD device decreases at lower photon energies.[32] We have also shown spectroscopic evidence that long-lived photoinduced charge transfer yields increase with higher photon-energy in blends of PbS QDs with poly(3-hexylthiophene-2,5-diyl) (P3HT).[34] While these results suggest that hot carriers in photoexcited PbS QDs promote more efficient hole transfer, they are only able to provide indirect evidence.

In this work, we directly probe hot hole transfer in a polymer/QD blend on timescales consistent with carrier cooling rates in the QDs. We build on previous steady-state photoinduced absorption (PIA) measurements, using the same P3HT/PbS-QD system.[34] The films in this study use postdeposition ligand exchange with halide ions to promote interfacial charge transfer and electronic coupling among the QDs. We selectively excite only the QDs in these samples at either 750 or 900 nm, and probe the resulting P3HT bleach in the visible region. Our results indicate that, per photon absorbed, the higher photon-energy (750 nm) pump yields a greater population of photoexcited holes transferred to the polymer at all timescales. Importantly, we show that the higher photon-energy pump has a significantly greater hole transfer yield appearing within the first several picoseconds than the lower energy excitation, providing direct evidence that excess energy above the QD bandgap can facilitate charge transfer to the polymer on timescales competing with carrier cooling.[101]

We prepared samples by blending poly(3-hexylthiophene-2,5-diyl) (P3HT) with PbS quantum dots (1:9 w/w ratio) in 1,2-dichlorobenzene, and spin casting the blend solution on glass substrates in a nitrogen glove box. A postdeposition ligand exchange was subsequently performed by pipetting a methanol solution of tetrabutylammonium iodide (TBAI) onto the surface of the film, and spinning dry after 30 s. TBAI was chosen over the previously reported 3-mercaptopropionic acid (MPA) treatment, as TBAI treatment showed improved signal and cleaner spectra in the transient absorption experiments. Sample films for transient absorption were encapsulated in a nitrogen glove box by adhering a glass cover slide to the sample film with epoxy.

4.2 EXPERIMENTAL DETAILS

4.2.1 *Sample Fabrication*

PbS quantum dots were synthesized using air-free Schlenk line techniques, following a modified version of the hot-injection synthesis reported by Hines and Scholes.[48] Briefly, the lead precursor was prepared in a 3-neck flask with PbO (450 mg), oleic acid (1.2 g), and 1-octadecene (14 g). The mixture was degassed at 100˚ C under continuous stirring for 1-2 hours, then placed under nitrogen flow and cooled to 75˚ C. The sulfur precursor was prepared in a separate 3-neck flask by degassing 4 g of 1-octadecene at room temperature for 20 min. The flask was then placed under nitrogen flow and 210 µL of bis(trimethylsilyl) sulfide $(TMS)_2S$ was added to the flask, and stirred to mix. The TMS solution was rapidly injected via syringe into the lead precursor flask and left on heat for 5 minutes. The heat was then turned off, and the flask was left to slowly cool to room temperature. The product was cleaned first by precipitation with acetone followed by centrifugation. The QDs were dispersed in a minimal amount of hexanes, and cleaned by precipitation followed by centrifugation, once with acetone, and twice with methanol. The precipitated QDs were then dried under nitrogen flow. A solution ligand treatment with butylamine was performed by dispersing the QDs in ~3 mL of butylamine, followed by sonication for 30 min. The QDs were precipitated with isopropanol and collected via centrifugation. This treatment was repeated once, and the final product was dried under nitrogen flow, transferred into a glove box, and dissolved in 1,2-dichlorobenzene (DCB).

Solutions of poly(3-hexylthiophene-2,5-diyl) (P3HT, Rieke Metals, P200) were prepared using a concentration of 40 mg/mL in DCB, and stirred at 65˚ C to dissolve. The polymer was then blended with the quantum dot solution in a 1:9 (w/w) ratio, and stirred for at least 1 hr. at 65˚ C. Prior to deposition, the blend solution was filtered to remove particulates (PTFE, 0.45 µm pore size). The solution was spin-cast on clean glass substrates at 2500 rpm for 60 s. Iodide ligand exchange was subsequently performed by coating the film surface with a tetrabutylammonium iodide (TBAI) solution (10 mM, in anhydrous methanol) while on the spin coater. After 30 s the samples were spun dry and rinsed once with methanol, and again dried by spinning. The samples were encapsulated in the glove box by adhering glass cover slides to the sample face with epoxy.

4.2.2 *Transient Absorption Measurements*

Time-resolved absorption measurements were conducted using an Ultrafast Systems Helios (UV-NIR) femtosecond transient absorption (TA) spectroscopy system. The Helios system utilizes fiber-coupled CMOS (350-800 nm) and InGaAs (800-1600 nm) spectrometers for visible and NIR detection, respectively. Pump and probe pulses were derived from the output of a Coherent Libra Ti:Sapphire regenerative amplifier (1 kHz, 50 fs) with an output of 4 mJ/pulse at 800 nm. A small portion of the Libra output was routed through a delay line, adjusted with neutral density filters and irises, and focused onto a sapphire crystal to generate white light continuum probe pulses. Separate crystals were used for visible and NIR probe pulses. The probe beam was split before reaching the sample to provide a reference signal, monitored with a separate detector to account for fluctuations in laser intensity. The 750 and 900 nm pump beams were generated with an optical parametric amplifier (Coherent OPerA Solo), and filtered with narrow (+/- 10 nm) band pass filters. The incident excitation intensities of the 750 and 900 nm pump beams were approximately 15 and 19 μJ/cm^2, respectively.

4.3 DISCUSSION

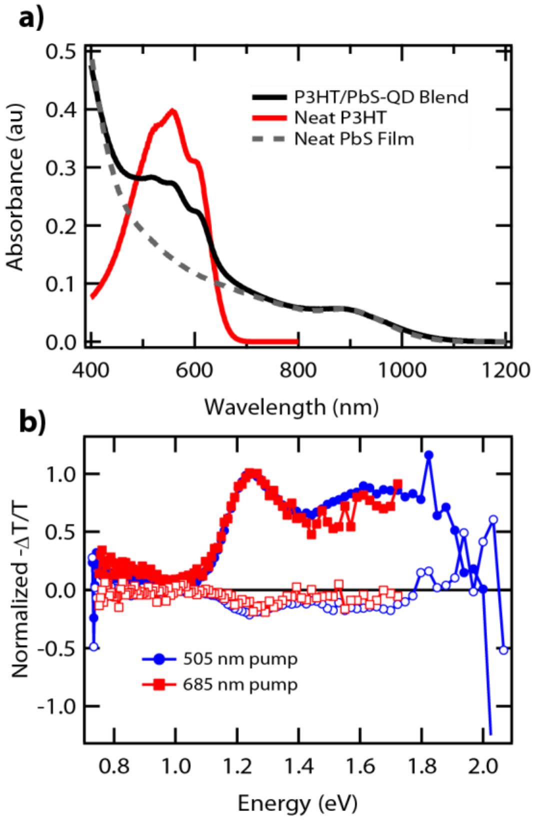

Figure 4-1. (a) Thin film absorbance spectra of a P3HT/PbS blend after postdeposition ligand exchange with TBAI (black), and neat P3HT (red) and PbS (gray, dashed) films. (b) Quasi-steady state photoinduced absorption spectra of a P3HT/PbS blend using 505 nm (blue circles) and 685 nm (red squares) excitation. Filled symbols represent the *x*-channel (in-phase) portion of the signal, and open symbols show the *y*-channel (out-of-phase) portion.

Figure 4-1a shows the absorbance spectra of a P3HT/PbS-QD composite film after ligand exchange with TBAI, along with the absorbance of both neat P3HT and PbS-QD films. The quantum dot first exciton peak appears at ~900 nm (1.38 eV), corresponding to ~3 nm diameter particles.[53, 111] We chose smaller PbS quantum dots because they yield a greater measureable signal compared to larger quantum dots in quasi-steady state photoinduced absorption (PIA) experiments on blends with P3HT.[34, 47] **Figure 4-1**b shows PIA spectra of such a P3HT/PbS composite film with both selective QD excitation, and excitation of both components, confirming that these iodide-passivated P3HT/PbS-QD composites undergo efficient charge transfer by measuring the long-lived (μs-ms) excited states on the polymer following photoexcitation. The low energy peak at 1.27 eV (980 nm) corresponds to the formation of polarons on the polymer chains, and we attribute the broad peak at ~1.65 eV (750 nm) to an electroabsorption (EA) feature, as previously reported for P3HT.[17, 34, 59] The data in **Figure 4-1**b show that selective excitation of only the quantum dots in the blend at 685 nm yields the same optical signatures of polarons on the polymer chains obtained when exciting both polymer and quantum dot components at 505 nm. These results show that, at long times, selective excitation of the *QD* component leads to the same *polymer* polaron species as direct excitation of the polymer.

To examine wavelength-dependence of hole transfer on the sub-picosecond timescale associated with carrier cooling in the PbS QDs, we used transient absorption (TA) spectroscopy to compare the hole transfer dynamics when exciting only the QD phase of the blend at both 750 and 900 nm. At sub-nanosecond timescales, the TA spectra in the NIR region are dominated by the bleaching of the first exciton transition of the QDs in the 800-1100 nm region (see Appendix C **Figure C- 1**a). This bleach directly overlaps with the polymer polaron absorption transition at ~980 nm, making it difficult to detect hole transfer to the polymer using this feature. Instead, we monitor the polymer ground state bleach in the visible region. While this signal partially overlaps with a competing QD feature, we are able to fit the data to extract the polymer bleach dynamics as discussed below.

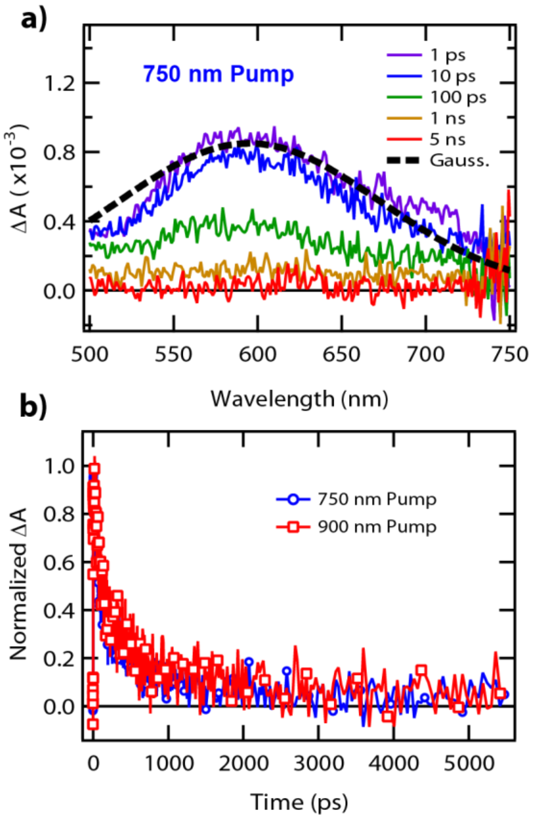

Figure 4-2. (a) Transient absorption spectra of a neat PbS-QD film excited at 750 nm, and (b) normalized kinetic traces of the QD induced absorption feature at 590 nm for data taken with 750 nm (blue circles) and 900 nm (red squares) excitation.

Figure 4-2a shows the TA spectra of a neat TBAI-treated PbS-QD film excited at 750 nm. The black dashed trace is a Gaussian function to approximate the QD spectra when fitting the TA spectra of the blend. The QDs exhibit an induced absorption feature in the visible region centered at ~590 nm which has previously been attributed to the red shift of higher energy bands induced by the presence of the 1S exciton.[102] Excitation at 900 nm yields the same spectral feature, shown in Appendix C, **Figure C- 1**. The kinetics of this feature, probed at the 590 nm maximum, are shown in **Figure 4-2**b for both 750 and 900 nm excitation. The signal shows the same behavior with both pump wavelengths, and decays completely between 1-2 ns. Because we aim to monitor the evolution of the P3HT ground state bleach in the same spectral region, we therefore account for this competing quantum dot induced absorption signal in measurements made on the polymer/QD blends.

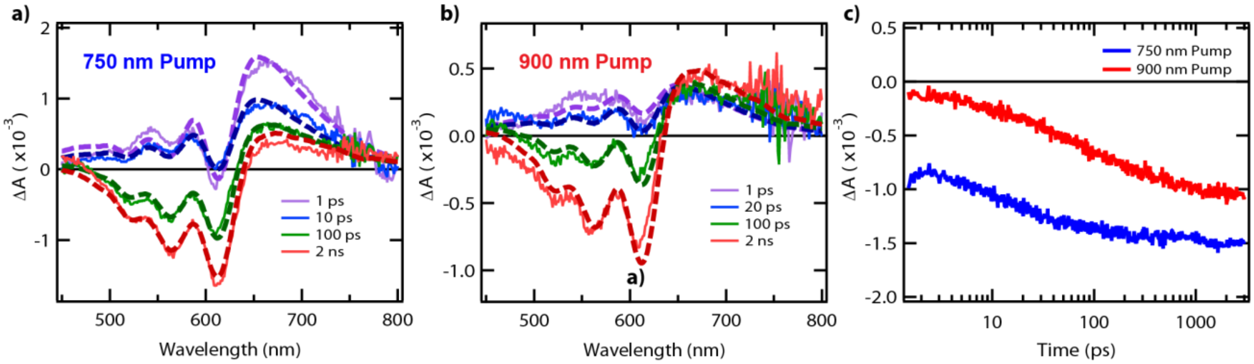

Figure 4-3. Transient absorption spectra of a P3HT/PbS-QD blend excited at (a) 750 nm and (b) 900 nm. Dashed lines indicate fits to the data. c) Kinetic traces of the polymer bleach signal (at 610 nm) extracted from the fits for 750 (blue) and 900 nm (red) excitation.

Figure 4-3a and b are the key data from this study, and show the TA spectra for the P3HT/PbS blend taken with 750 and 900 nm photoexcitation, respectively. Both spectra show peaks corresponding to the polymer bleach in the range of 450-630 nm. The PIA feature in the polymer spectrum at ~670 nm has been previously attributed to contributions from more delocalized polarons[112] and electroabsorption at the band edge.[113] The spectra at longer (ns) time delays, after the quantum dot PIA feature has predominantly decayed, are similar between the two different pumps as shown in Appendix C **Figure C- 2**. The polymer bleach arises from depopulation of the polymer ground state by hole transfer from the PbS quantum dots. We verify that the 750 nm pump does not directly excite the polymer by showing that a neat P3HT film pumped at this wavelength does not yield TA signal from the polymer ground-state bleach (see Appendix C **Figure C- 3**). We emphasize that, because the polymer has a higher bandgap than the PbS quantum dots, and because only the QDs were excited, observation of a polymer bleach provides convincing evidence of charge transfer from QD to polymer.

In addition to the polymer bleach, both spectra show some contribution at early times from the QD induced absorption discussed above (**Figure 4-2**). We therefore fit the data in **Figure 4-3**a and 4-3b as a linear combination of the P3HT bleach and PbS induced absorption (dashed lines in **Figure 4-3**a and b). The resulting fits describe the spectra well at all but the earliest times (< 1 ps). The reference spectra used for the fitting are shown in Appendix C **Figure C- 4**, along with the raw spectra from which they are derived. At times earlier than 1 ps, the spectra cannot be represented as a simple superposition of long-time polymer bleach and QD induced absorption

(Appendix C **Figure C- 5**), suggesting that additional species may be present at these earliest times. The fit residuals are significantly greater within the first several hundred fs than at times >1 ps, after which the fits accurately represent the data. In addition to the instrument response during the first few hundred fs, the QD induced absorption is also evolving as the carriers cool. Correlated electron/hole pairs might also form at the QD/polymer interface and evolve at early times, as have been proposed to explain some features in polymer/fullerene blends,[114] but would require significant additional study in these QD/polymer blends. Probing the dynamics on the sub-ps timescales should thus prove interesting for future studies.

Figure 4-3c compares the kinetic traces of the polaron (polymer bleach signal) for data obtained with 750 and 900 nm excitation, after removing contributions from the quantum dot feature. The raw data for these traces is shown in Appendix C, **Figure C- 6**. The pump intensities were adjusted to produce matched excitation densities, enabling quantitative comparison of the relative signal magnitudes. **Figure 4-3**c shows that the 750 nm pump produces a larger polymer bleach, indicative of greater hole transfer yields from the photoexcited QDs to the polymer. This result is consistent with our previous steady-state results with PIA indicating larger photoinduced carrier populations at higher excitation photon energies.[34] At longer times, the dynamics of the polymer bleach signal are similar for both pump wavelengths. We note that the signal grows in over the course of the first few hundred picoseconds, and reaches a plateau by ~1 ns. These slower dynamics of the relaxed carriers at longer times are consistent with the relatively slow (picosecond-nanosecond) hole transfer rates observed from CdSe QDs to a hole-accepting solution-processable polyphenylenevinylene derivative (MDMO-PPV).[110]

Importantly however, the higher energy (750 nm) pump exhibits a significant yield of prompt hole transfer to the polymer at times as early as 1 ps, with roughly 60% of the signal appearing at early times, and the remaining 40% growing in over longer times. In contrast, excitation of the sample at 900 nm shows minimal signal at 1 ps time delay, with almost all of the polaron-induced polymer bleach growing in over the first nanosecond. This dramatic difference in early-time yields between the two excitation photon energies provides direct support for the hypothesis that hot hole transfer accounts for the differences in yield of long-lived charges in blends of quantum dots and conjugated polymers. Based on the UV-Vis spectra of the PbS QDs, the 750 nm pump should excite the tail of the QD $1P_h$-$1P_e$ transition, or the symmetry forbidden $1P_h$-$1S_e$ transition in the QDs, both of which should produce hot holes, while the 900 nm pump primarily excites the lowest energy first exciton ($1S_h$-$1S_e$) transition.[111, 115-116] We speculate that the higher photon-energy pump may produce more rapid charge transfer either because the excess energy facilitates the structural distortion associated with polaron formation on the polymer,[95, 117] or because shorter wavelength excitation produces higher energy holes on PbS that are more delocalized, and thus leak out further into the polymer matrix.[103, 118] In either case, these results provide important confirmation that most of the charge transfer events to the polymer following higher energy excitation occur within the timescale of carrier cooling in PbS QDs, and that hole transfer from carriers in relaxed states on the QDs to the polymer is comparatively slow. Future studies should also seek to differentiate between the effects of excess energy of the hot carriers, and the indirect effect of excess energy on the delocalization of the hole wavefunction on the QD, perhaps by varying both the QD size and systematically varying the excitation energy. Studies with additional polymer hosts with different frontier energy levels, and different degrees of structural rigidity and reorganization energy would also be interesting to explore the coupling between driving force and reorganization energy.[119]

4.4 CONCLUSION

In summary, we present transient absorption measurements on a model P3HT/PbS-QD blend that shows a greater yield of photoinduced hole transfer with higher energy excitation. While the behavior between the two pump wavelengths is similar at longer timescales, the higher energy pump exhibits a greater prompt overall yield of holes on the polymer, notably in the first several picoseconds. This result provides direct spectroscopic evidence that hot carriers on the quantum dots facilitate charge transfer to the polymer, leading to improved free carrier generation. These findings show that both hot and relaxed carriers can be transferred from QDs to a host polymer, albeit at different timescales and with different efficiencies, and inform the design requirements of polymer/QD solar cells and hot carrier collection schemes.

Chapter 5. CONCLUSIONS AND FUTURE WORK

The work in this thesis has shown significant progress toward understanding the factors regulating free carrier generation and recombination in polymer/quantum dot solar cells. The study detailed in Chapter 2 examined the effect of postdeposition ligand exchange on polymer/QD device performance. We found that different QD surface ligands influence device performance primarily through changes open-circuit voltage and fill factor, with 3-mercaptopropionic acid (MPA) treatment resulting in the highest devices efficiency, and iodide treatment the lowest. Photoinduced absorption (PIA) and transient photovoltage experiments both demonstrate that ligand treatments with better device efficiency exhibit longer carrier recombination lifetimes and greater long-lived carrier populations under open-circuit conditions. These findings indicate that QD surface chemistry plays an important role in controlling bimolecular recombination losses that reduce device V_{OC}. We attribute the improved device performance with MPA treatment in part to the greater observed mobility-lifetime products of photogenerated charge carriers observed with this ligand treatment in neat PbS quantum dot films.[57] Furthermore, we speculate that the reduced V_{OC} and fill factor observed with halide ions may partially result from the dipole-induced shift in QD band levels relative to the polymer energy levels with halide treatment.

This study demonstrates the challenge and opportunity of using QD surface modification to enhance polymer/QD device properties. The differences in solar cell performance in this study are in contrast to QD-only devices with PbS, where halide ligand treatments exhibit some of the best device performances to date.[29-30] This indicates that in addition to effective trap state passivation and high mobility-lifetime products for carriers generated within the QDs, polymer/QD devices have the added requirements of finding ligand treatments that result in favorable energy level alignment with the donor polymer and promote longer bimolecular recombination lifetimes at open-circuit. Future studies should seek to understand the role of dipole-induced band level shifts, perhaps by using a more systematic series of ligands such as various benzenedithiol derivatives. Additionally, investigating the differences in these ligand exchanges using electron tomography would be useful in determining whether some of the differences observed in this work are related to film morphology following postdeposition ligand exchange.

The work in Chapters 3 investigated the role of hole transfer in polymer/QD blends. We used PIA to show that selective excitation of the quantum dot component yields the optical signature of long-lived charge carriers on the polymer, providing direct evidence that photoexcited QDs are able to generate free carriers via hole transfer to the polymer. While this supports the hypothesis that polymer/QD blends operate as bulk heterojunctions, other work from our group suggests that in some cases these blends may operate as partial Schottky-diode solar cells, in which excitons on the QD phase may directly yield free carriers independent of the polymer.[33, 37] The degree to which these mechanisms are responsible for the overall carrier generation in devices is currently unknown, and likely depends on properties of the donor polymer, quantum dot ligands, and film morphology. Future studies should seek to determine the factors that regulate these mechanisms of device operation by studying hole transfer and energy transfer yields in blends using donor polymers with different frontier energy levels, and varying QD sizes.

Additionally, we found that excitation of both polymer and QD species with a higher photon-energy pump resulted in greater polaron yields than lower photon-energy excitation, where the QDs were selectively excited. This observation indicates that hot carriers on the QDs may facilitate more efficient hole transfer. The study in Chapter 4 used TA spectroscopy to probe the photon-energy dependence of hole transfer in polymer/QD blends on the subpicosecond timescales of carrier cooling in the QDs. We showed that higher pump photon-energy exhibits a substantially greater prompt hole transfer yield to the polymer compared to lower photon-energy excitation, demonstrating that the excess energy associated with the higher photon-energy pump facilitates greater hole transfer efficiency to the polymer. We also determined that relaxed carriers have relatively slow transfer rates and reduced efficiency. Future work should focus on distinguishing between the influence of the excess energy of hot carriers from the concomitant effect of increased hole delocalization, by varying both QD size and excitation energy. Furthermore, studying the relationship between the polaron yields with different photon-energy pumps and device internal quantum efficiency in blends using polymer hosts with different frontier energy levels would provide insight into the role of energetic driving force in achieving free carrier generation. In conclusion, polymer/QD composites offer a promising route for next-generation solar cells and photodetectors, that are compatible with low-cost manufacturing techniques such as roll-to-roll printing. This work provides insight into the relationship between device performance and QD surface chemistry, as well as a more complete understanding of the operational mechanisms and factors influencing free carrier generation in polymer/QD blends.

APPENDIX A: SUPPORTING INFORMATION FOR CHAPTER 2

A1. PHOTOINDUCED ABSORPTION

Figure A- 1 shows both X- and Y-channel PIA data for samples exhibiting PIA signal. Although the MA ligand exchanged devices show negligible photocurrent generation, the PIA data for MA shows substantial generation of long-lived polarons on the polymer chains.

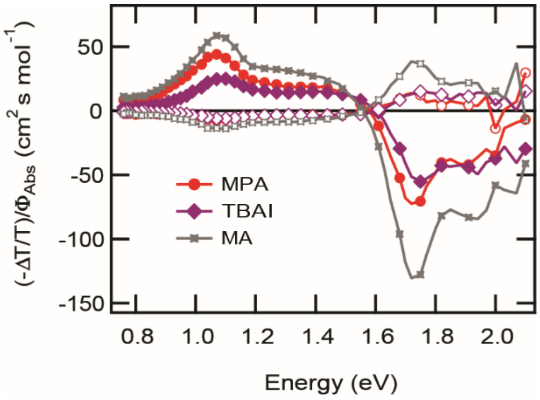

Figure A- 1. Quasi-steady state PIA spectra of PTB1/PbS QD films treated with MPA (red), TBAI (purple), and a malonic acid (gray). Filled symbols represent *x*-channel data and unfilled symbols represent *y*-channel data.

A2. LIGAND EXCHANGE PROCESSES

Preparation of solar cells in this study involved a two-step ligand exchange process. The first step was a solution-based treatment with butylamine (BAm) performed prior to mixing with the polymer (see Experimental section of the main text). The second step is the post-deposition ligand exchange involved in this study. **Figure A- 2** compares the external quantum efficiency (EQE) of devices fabricated either using as-synthesized oleic acid capped QDs (PbS-OA) or BAm-treated QDs (PbS-BAm). Devices fabricated using PbS-OA and a post-deposition ligand exchange with MPA show low EQE and short-circuit photocurrent (J_{SC}). Devices incorporating PbS-BAm with no post-deposition ligand exchange show similar low EQE, and the devices also suffer poor diode rectification. However, devices using PbS-BAm in addition to post-deposition ligand exchange with MPA have significantly enhanced photocurrent and good diode behavior. These data show the importance of utilizing both solution-based ligand treatment with BAm, as well as post-deposition ligand exchange on the polymer/QD film.

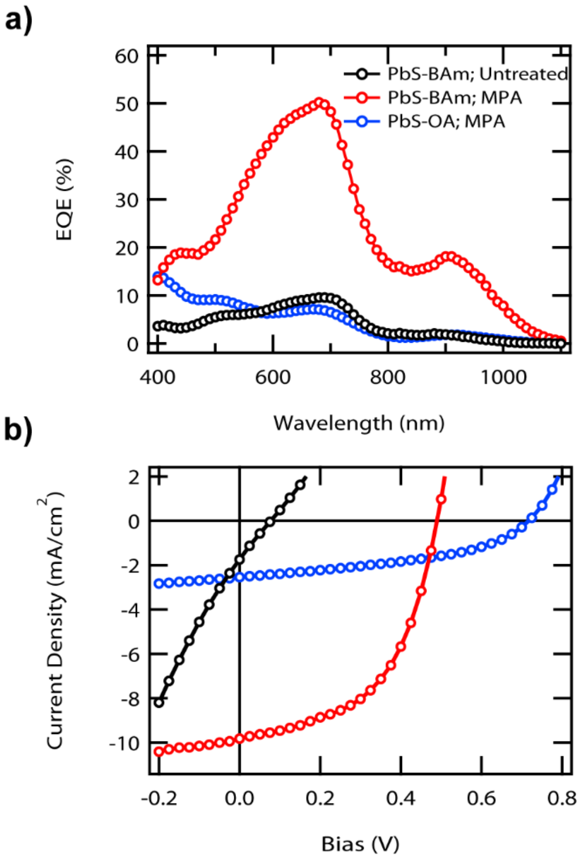

Figure A- 2. a) External quantum efficiency (EQE) values for devices fabricated with PbS-OA and post-deposition treatment with MPA (blue), PbS-BAm with no post-deposition treatment (black), and PbS-BAm after post-deposition ligand exchange with MPA (red). b) *J-V* characteristics of the same devices under AM 1.5 simulated solar illumination.

A3. LIGAND EXCHANGE VERIFICATION

We verify ligand exchange using attenuated total reflectance infrared spectroscopy performed films of neat PbS QDs, by observing reduced intensity of C-H stretching modes following ligand exchange as shown in **Figure A- 3**. The vibrations at 2925 cm^{-1} and 2854 cm^{-1} are assigned to ν_{asym} (C-H) and ν_{sym} (C-H), respectively. Each QD film was prepared on a glass substrate under identical conditions. The apparent decrease in these vibrational modes indicate effective removal of native oleate ligands following the ligand exchanges used in this study.

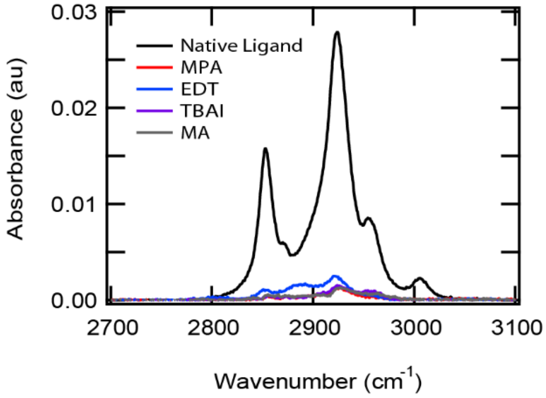

Figure A- 3. Infrared analysis of PbS QD films untreated (black) and after ligand exchange with MPA (red), EDT (blue), TBAI (purple), malonic acid (gray).

A4. CHARGE CARRIER DENSITY CORRECTIONS

The measured charge carrier density values (*n*) were corrected for losses due to charge recombination during charge extraction (CE). This is necessary because the bimolecular recombination lifetimes approach the same timescale as the lifetime for charge extraction from the device at high light intensities (≥ 100 mW/cm^2) as shown in **Figure A- 4**a. The losses in carrier density that occur over the course of CE are calculated using the quantum yield (QY) for charge extraction according to the equation

$$QY = \frac{\frac{1}{\tau CE}}{\frac{1}{\tau TPV} + \frac{1}{\tau CE}}$$

where τ_{TPV} is the carrier recombination lifetime measured with TPV and τ_{CE} is lifetime of the corresponding CE transients. The measured values of *n* are subsequently divided by the QY to correct for recombination losses that occur over the timescale of CE. We assume τ_{TPV} to be constant, likely leading to over-estimates of losses due to recombination when τ_{TPV} is fast. This is because the rate of recombination decreases (τ_{TPV} increases) during the course of charge extraction, as the carrier concentration is depleted. The original and corrected data are shown in **Figure A- 4**b and c, respectively.

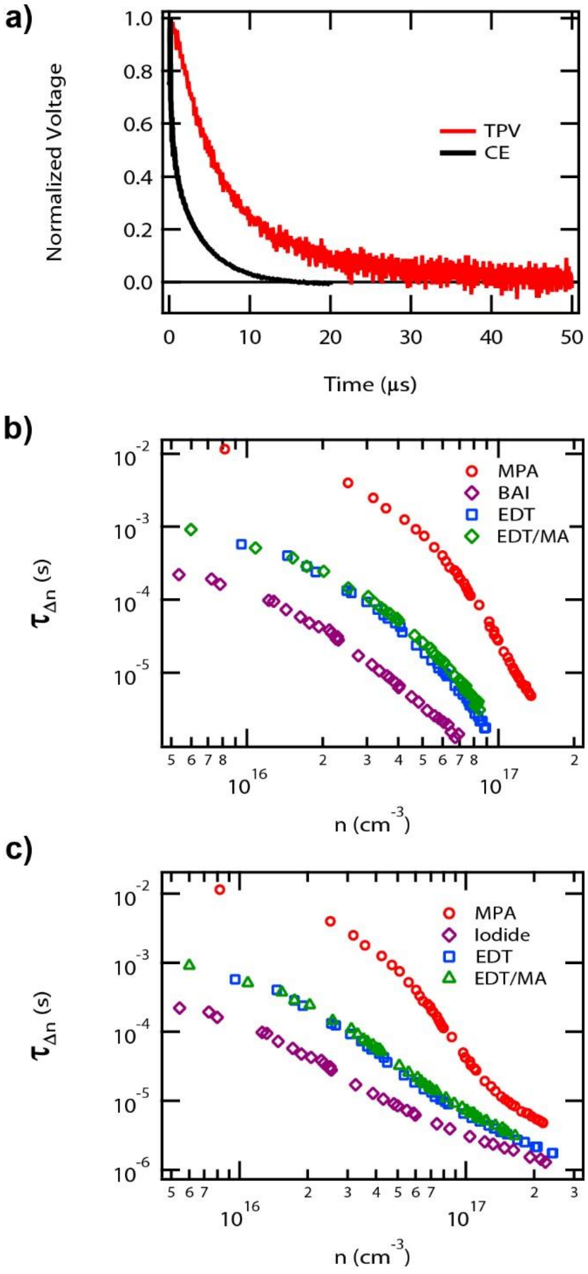

Figure A- 4. a) Normalized voltage transients for TPV (red) and CE (black) for a MPA-treated device under the same background white light illumination (~300 mW/cm^2), and comparison of small perturbation charge carrier recombination lifetime ($\tau_{\Delta n}$) vs charge carrier density *n*, before (b) and after (c) correcting for losses incurred during carrier extraction.

A5. LIGAND EXCHANGE CONTROL

We verify the ligand exchanges we perform in this study are not chemically altering the polymer by measuring the steady-state absorbance spectra of neat polymer films treated with the ligand exchange solutions as shown in **Figure A- 5**. We see no changes in film absorption after the ligand treatment relative to the untreated film.

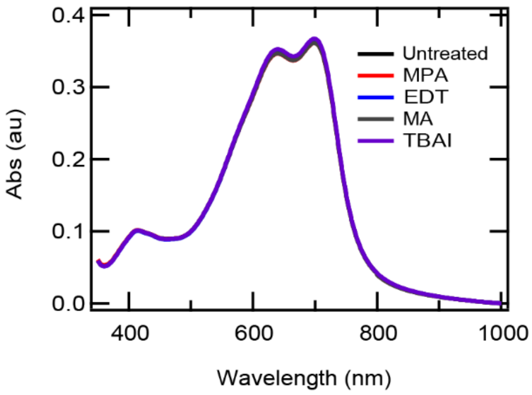

Figure A- 5. Absorbance spectra of neat PTB1 films before and after treatment with ligand exchange solutions.

A6. *J-V* CHARACTERISTICS OF ALL DEVICES

The J-V characteristics of malonic acid (MA)-only treated devices are compared to the other ligands used in this study in **Figure A- 6**. The MA-only devices show poor rectification and little photocurrent under illumination, making it too difficult to perform TPV and CE measurements.

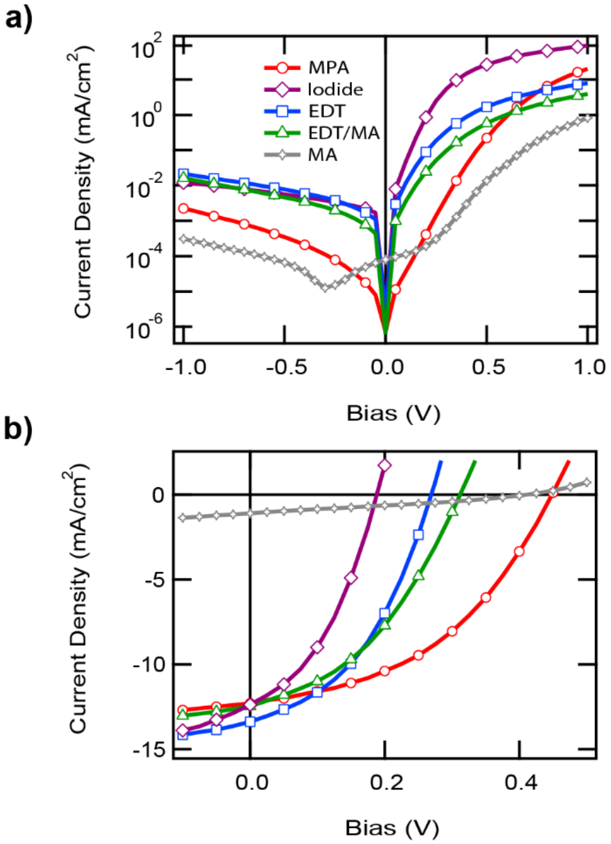

Figure A- 6. (a) Dark and (b) light *J*-*V* curves for PTB1/PbS QD devices subject to different ligand exchanges: MPA (red circles), TBAI (purple diamonds), EDT (blue squares), and a 1:1 mixture of EDT/MA (green triangles), and MA (gray stars).

A7. ENERGY LEVEL DIAGRAM

The net surface dipole of the PbS QDs is determined by the difference between the intrinsic dipole of the ligand and the interface dipole between the QD surface atoms and the ligand molecules. The change in surface dipole of the QDs shifts the vacuum level, and the valence band (VB) and conduction band (CB) levels of the QDs, accordingly. Both band edges are shifted by the same energy, so the QD band gap remains unaffected. Here we use values for the QD valence band reported by Brown *et al*., and approximate the conduction band values by adding the optical band gap of the QDs (E_g^{opt} = 1.38 eV) used in this study. **Figure A- 7** compares the band levels of the PTB1 polymer with those of PbS QDs with different surface ligands. A rough estimate for the possible device open-circuit voltage can be determined from the difference between the ionization potential of the donor species (polymer) and the CB of the acceptor species (PbS QDs). This energy difference (and the upper estimate for device V_{OC}) is reduced with increasing net surface dipole (MPA < EDT < TBAI).

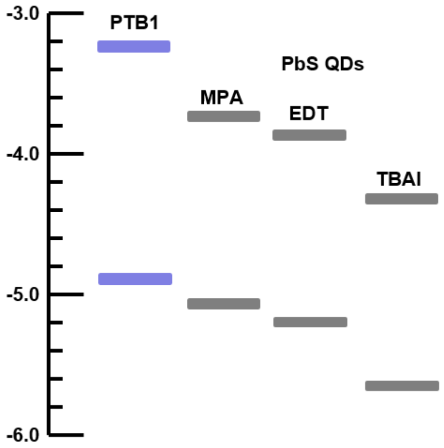

Figure A- 7. Energy level diagram for the band edges of PTB1 polymer and PbS QDs treated with the different ligands used in this study as reported in the literature, obtained using cyclic voltammetry (CV) and ultraviolet photoelectron spectroscopy (UPS), respectively.

A8. DEPENDENCE OF J_{SC} ON LIGHT INTENSITY

The dependence of device short-circuit current on incident light intensity for all ligand treatments are shown in **Figure A- 8**. The fit parameters (α) are shown in **Table A- 1**. This data shows similar characteristics for all ligand treatments, demonstrating that the QD surface ligand has little effect on the recombination dynamics at short-circuit. The deviation of α from unity shows that there are small non-first order recombination dynamics that occur at short circuit for these devices.

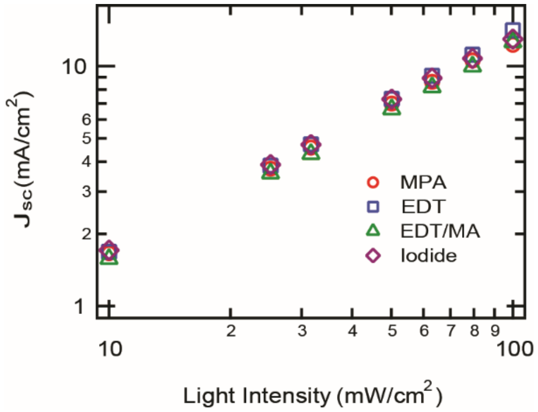

Figure A- 8. Dependence of J_{SC} on incident light intensity for devices (shown without fits) treated with MPA (red circles), EDT (blue squares), EDT/MA (green triangles), and iodide (purple diamonds).

Table A- 1. Average Values for the Fit Parameter α[a]

ligand exchange	**average α**
MPA	0.90 ± 0.01
EDT	0.91 ± 0.01
EDT/MA	0.90 ± 0.01
Iodide	0.88 ± 0.01

[a] The values reported are the averages and standard deviations of the mean from four pixels, each from different devices.

APPENDIX B: SUPPORTING INFORMATION FOR CHAPTER 3

B1. PDTPQX-HD SYNTHESIS

Poly(2,3-bis(2-(hexyldecyl)-quinoxaline-5,8-diyl-*alt*-N-(2-hexyldecyl)-dithieno[3,2-b:2′,3′-d]pyrrole) (PDTPQx-HD) was synthesized as reported previously.[17] The polymer structure is shown below.

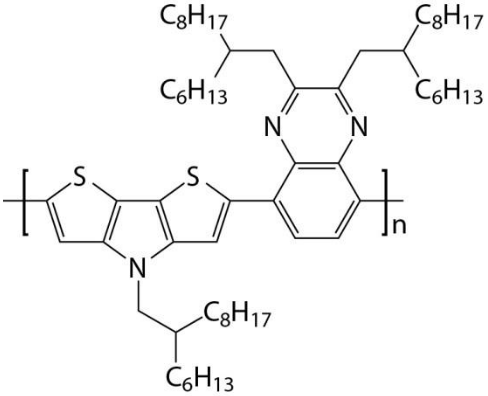

Figure B- 1. Chemical structure of PDTPQx-HD

B2. ABSORBANCE OF PDTPQX-HD/PC$_{61}$BM

Supporting information **Figure B- 2** shows the thin film absorbance of the PIA sample used to obtain the data in **Figure 3-3**a of the text. The sample shows no absorbance for energies lower than ~1.4 eV, resulting in the lack of signal in the PIA spectrum for this sample when excited at 1.27 eV.

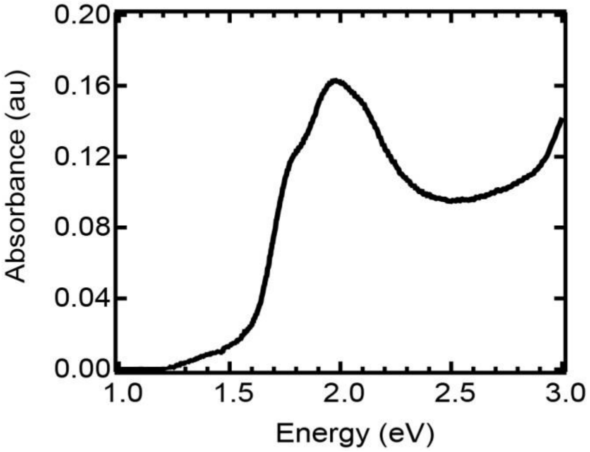

Figure B- 2. PDTPQx-HD/PC$_{61}$BM thin film absorbance spectrum. The sample consisted of a 1:1 (w/w) ratio bulk heterojunction blend of PDTPQx-HD/PC$_{61}$BM.

B3. MODULATION-DEPENDENCE OF POLARON AND ELECTROABSORPTION FEATURES

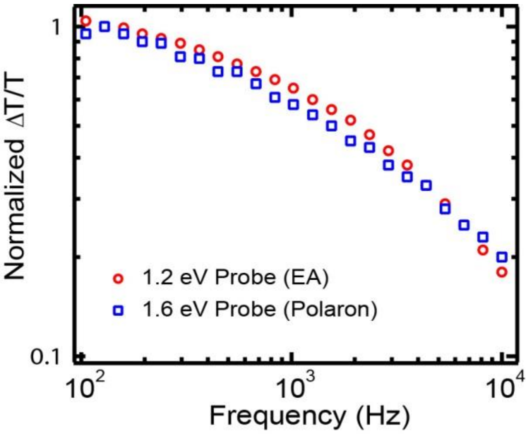

Figure B- 3. Modulation dependence of the 1.6 eV (blue squares) electroabsorption and 1.2 Ev polaron (red circles) spectral features of a PDTPQx-HD/PCBM blend under 2.77 eV excitation.

B4. NORMALIZED IN-PHASE AND QUADRATURE PIA SPECTRA OF PDTPQX-HD/PBS

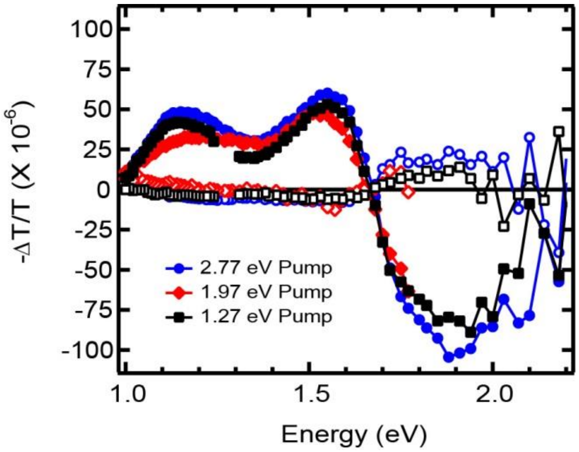

Figure B- 4. Un-normalized PIA spectra of the PDTPQx-HD/PbS sample from Figure 3-3b in the main text, acquired under 2.77 eV (blue circles), 1.97 eV (red diamonds), and 1.27 eV (black squares) excitation. Filled symbols correspond to X-channel (in-phase) signal and hollow symbols represent Y-channel (quadrature) signal. No significant changes in lineshape or the ratio of X-channel to Y-channel signal occur between the different excitation energies.

B5. THIOL TREATMENT OF PDTPQX-HD/PCBM AND NEAT PDTPQX-HD: NO SIGNIFICANT CHANGES IN PIA SPECTRA

To ensure that the post-deposition 3-mercaptopropionic acid (MPA) treatment of the PDTPQx-HD/PbS samples did not cause significant morphological changes or chemical doping of the polymer phase, we treated PDTPQx-HD/PCBM and neat PDTPQx-HD films with a 1 mM solution of MPA in anhydrous methanol. **Figure B- 5**a shows that the PIA spectrum of PDTPQ-HD/PCBM is not affected by the thiol treatment. Accordingly, modulation-dependence of the polaron feature shown in **Figure B- 5**b shows no significant differences in recombination lifetime resulting from MPA treatment. Furthermore, the neat polymer also shows no effects from the thiol treatment in the PIA and absorbance spectra as shown in **Figure B- 5**c and B-5d, respectively.

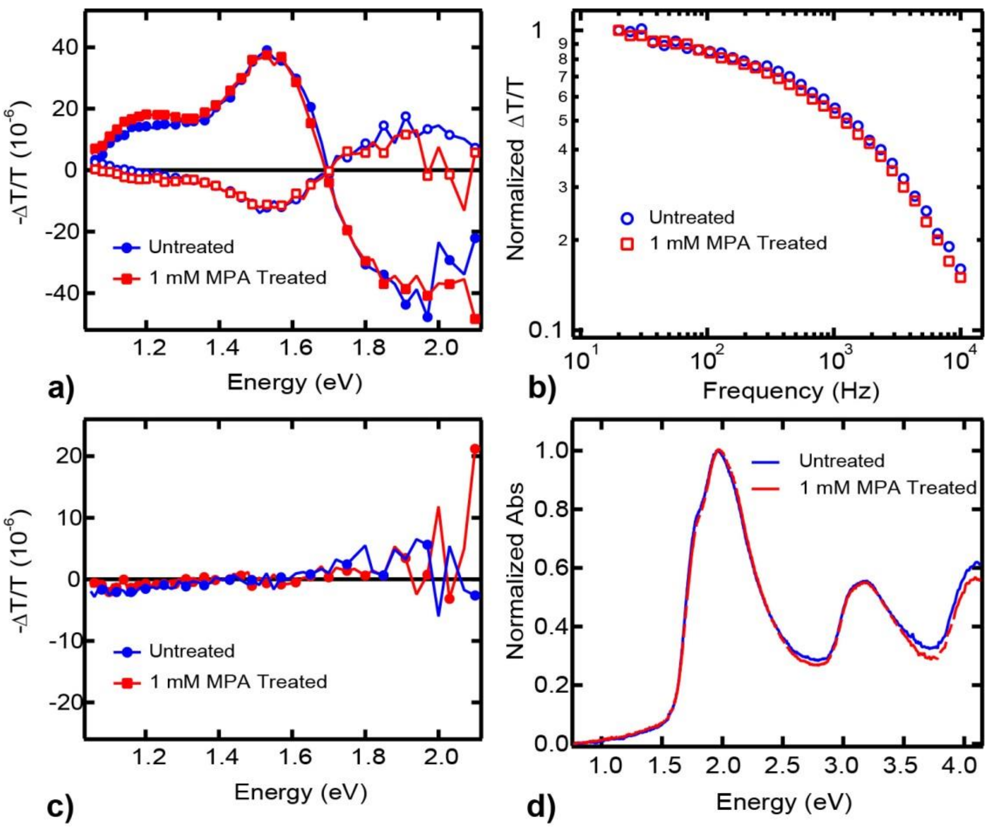

Figure B- 5. (a) PIA spectra of PDTPQx-HD/PCBM before (blue circles) and after (red squares) MPA-treatment. Filled symbols represent the X-channel (in-phase) portion of the data, and unfilled symbols represent the Y-channel (quadrature) portion of the data. (b) Modulation-dependence of PDTPQx-HD/PCBM before (blue circles) and after (red squares) MPA-treatment. (c) X-Channel PIA and (d) absorbance spectra of neat PDTPQx-HD before (blue lines) and after (red lines) MPA-treatment.

B6. PHOTOINDUCED ABSORPTION OF NEAT PBS

Figure B- 6 compares the PIA spectra of neat solution halide-treated PbS quantum dots before and after post-deposition treatment with 1 mM MPA against the PIA spectrum of a PDTPQx/PbS. A weak bleach feature can be seen at the optical band gap of the quantum dots (~1.07 eV), corresponding to bleaching of the first excitonic transition (^1S_h to ^1S_e). The magnitude of the signal is seen to increase slightly following MPA treatment. The quantum dot bleach overlaps the shoulder of the PDTPQx-HD polaron transition, and is therefore not observed in the polymer/quantum blend PIA spectrum.

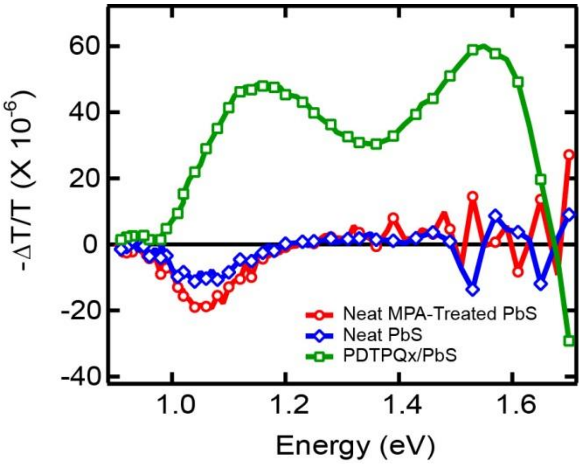

Figure B- 6. X-channel PIA spectra of neat (solution TBAI-treated) PbS before (blue diamonds) and after MPA-treatment (red circles), and MPA-treated PDTPQx-HD/PbS (green squares) under 2.77 eV excitation.

B7. DETERMINATION OF POLARON LIFETIMES FROM PIA PUMP MODULATION-DEPENDENCE

The dependence of PIA signal on pump modulation frequency can be used to determine an average polaron lifetime. **Figure B- 7** displays traces for the three different pumps (2.77 eV, 1.97 eV, and 1.27 eV) fit using the dispersive recombination equation shown in the figure inset.[17, 59] The dispersive fit parameters are nearly identical for the three different curves, with nearly identical lifetime (τ) distributions of τ ≈ 0.25 ms, and dispersion parameters (γ) or γ ≈ 0.67.

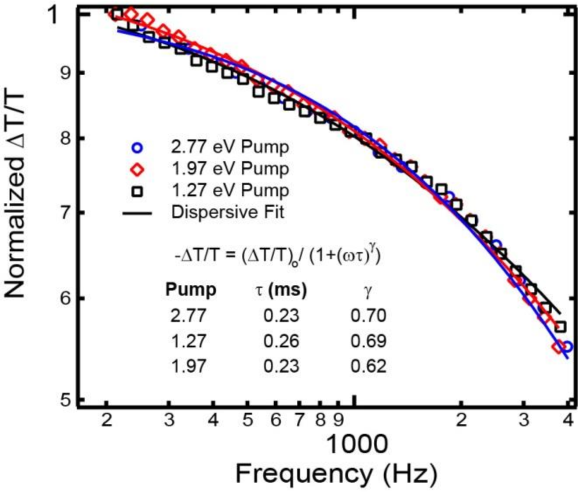

Figure B- 7. Modulation frequency dependence of the PIA signal (ΔT/T) monitored at the 1.85 eV polaron transition with varying pumps: 2.77 eV (blue circles), 1.97 eV (red diamonds), and 1.27 eV (black squares). Fit parameters (τ and γ) were determined by dispersive fits of the data to the inset model (solid lines) as a function of modulation frequency $f = \omega/(2\pi)$.

B8. CALCULATION OF RELATIVE POLYMER AND QUANTUM DOT POLARON YIELDS

Figure B- 8a shows the dependence of the polaron PIA signal magnitude, $R = ((X^2 + Y^2)^{1/2})$, on absorbed pump flux for PDTPQx-HD/PbS with 1.27 and 1.97 eV excitation. The relative pump power at each point was determined by measuring the photocurrent of a calibrated silicon photodiode through an aperture cut to the *probe* spot size. The pump spot size was larger than the probe spot size, and therefore, only the portion of the pump spot overlapping the probe beam was measured. The relative flux (photons/s) was then calculated using the calibrated diode’s spectral responsivity and the known pump photon energy. The total absorbed photons per second (Φ_{Abs}) for each pump intensity was subsequently determined based on the photon flux and the film optical density at the corresponding excitation wavelength.

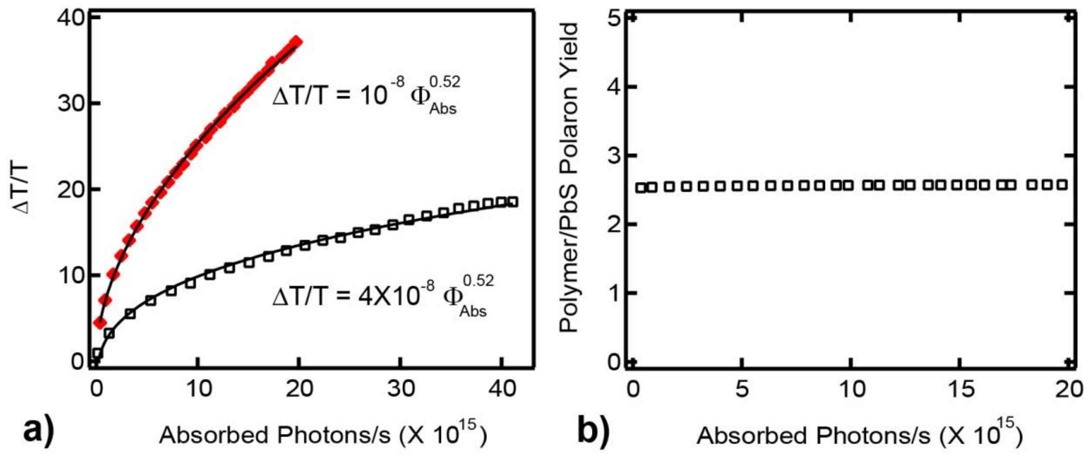

Figure B- 8. (a) Dependence of the PIA signal on absorbed pump photon flux (Φ_{Abs}) for the PDTPQx/PbS polaron transition under 1.97 eV (red diamonds) and 1.27 eV (black squares) excitation. The data were fit with power law curves, with the fit equations inset under the respective curve. (b) Ratio of polaron yields from polymer and quantum dot light absorption under 1.97 eV excitation, calculated at varying absorbed photon flux.

Figure B- 8b shows that the calculated ratio of polaron yields (ΔT/T per photons/s absorbed) generated from polymer and quantum dot components remains constant with changing excitation intensity. The 1.27 eV pump data was interpolated at each measured value of the 1.97 eV pump to compare the ΔT/T values for the two different pumps *with the same number of absorbed photons*. **Figure B- 9** shows the absorbance spectra of the quantum dots and polymer/quantum dot blend (in solution), normalized to the quantum dot exciton peak. The difference between the two spectra was used to determine the fraction of photons from the 1.97 eV pump absorbed by the quantum dot species. As discussed in the text, we assume that the observed polaron yield is independent of the excitation wavelength. Since the polaron signal generated by 1.27 eV excitation originates only from quantum dot absorption, we used the interpolated 1.27 eV pump data and the percentage of quantum dot light absorption at 1.97 eV to calculate the expected quantum dot polaron yield under 1.97 eV illumination (for small values of ΔT/T, ΔT/T is directly proportional to the absorbance). The polymer polaron yield was then determined using the difference between the total PIA signal and the calculated quantum dot polaron yield.

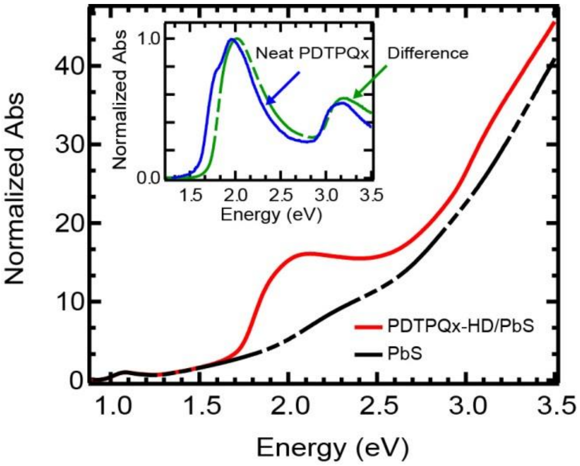

Figure B- 9. Absorbance spectra of the PDTPQx-HD/PbS blend solution (used to fabricate films for device and PIA data) (red line) and the PbS quantum dots (dashed black line) in tetrachloroethylene, normalized to the quantum dot exciton peak. The inset compares the normalized absorbance of neat PDTPQx-HD (blue line) to the difference spectrum of the blend and quantum dots (dashed green line).

B9. ENERGY LEVEL DIAGRAM

We determined the driving force for photoinduced electron transfer using the excited state ionization energy (the potential necessary to oxidize the photoexcited material) of the polymer donor species as described in the literatue.[78] We calculate the polymer excited state ionization energy ($IE_{(\mathrm{M+}/\mathrm{M*})}$) from the ground state ionization energy $IE_{(\mathrm{M+}/\mathrm{M})}$ and the singlet exciton energy E_g^{Opt} according to Equation 1 below.

$IE_{(\mathrm{M+}/\mathrm{M*})} = IE_{(\mathrm{M+}/\mathrm{M})} + \mathrm{E_g^{Opt}}$ (1)

This approximation accounts for the binding energy of the exciton, considering the driving force for charge separation (ΔE_{elec}) in terms of exciton dissociation to a ground-state acceptor, according to Equation 2.

$\Delta E_{elec} = EA_{(\mathrm{M}/\mathrm{M-})}$ [Acceptor] - $IE_{(\mathrm{M+}/\mathrm{M*})}$ [Donor] (2)

This approximation is not used for the hole transfer process due to the low exciton binding energy of the inorganic nanocrystals. In this case, the driving force for charge separation (ΔE_{hole}) was approximated by the energy difference of the polymer and quantum dot ground state ionization energies. **Figure B- 10** shows the estimated energies for determining the driving force of photoinduced charge separation. We calculate the driving forces for electron and hole transfer to be -0.52 eV and -0.27 eV, respectively.

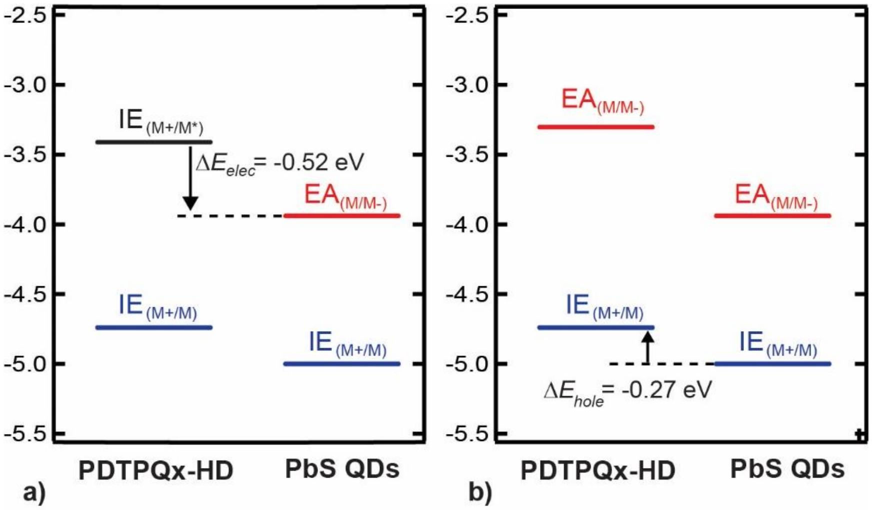

Figure B- 10. Energy levels for calculating the driving force for photoinduced (a) electron transfer and (b) hole transfer in PDTPQx-HD/PbS composites. The black line indicates the donor excited state ionization energy ($IE_{(M+ /M*)}$), blue lines represent ground state ionization energies ($IE_{(M+ /M)}$), and thin red lines show ground state electron affinities ($EA_{(M /M-)}$).

APPENDIX C: SUPPORTING INFORMATION FOR CHAPTER 4

C1. NEAT PBS QD TRANSIENT ABSORPTION DATA

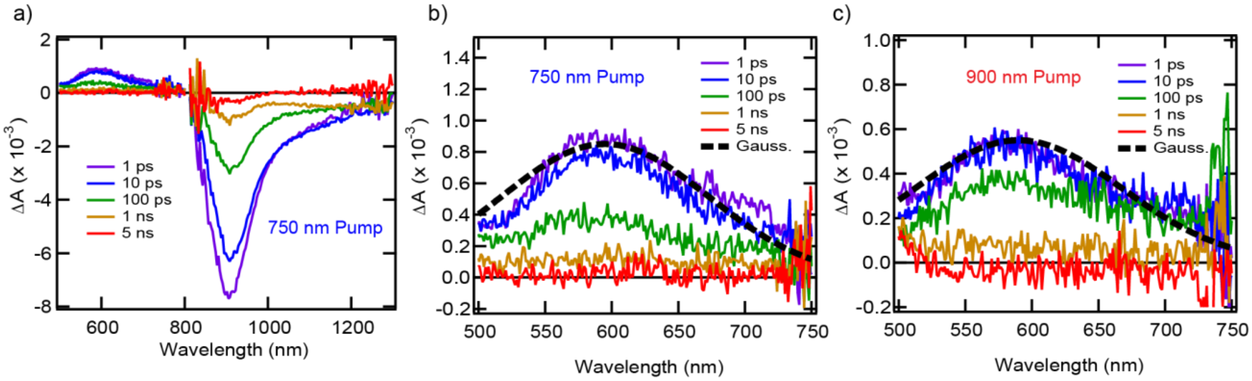

Figure C- 1. Transient absorption spectra of a neat PbS quantum dot film. (a) Visible and NIR spectra under 750 nm excitation, and visible region spectra excited at (b) 750 nm and (c) 900 nm.

Figure C- 1a shows the TA spectra of a neat PbS-QD film post-deposition treated with tetrabutylammonium iodide (TBAI) in the visible and near infrared (NIR) regions using 750 nm excitation. The prominent feature in the NIR region is attributed to a bleaching of the quantum dot first exciton transition ($1S_h$-$1S_e$). **Figure C- 1**a and C-1b compare the TA spectra in the visible region of the neat QD film excited at 750 and 900 nm, respectively. The QD spectrum in this region does not show dependence on pump photon energy. Black dashed traces show the Gaussian approximation to the data used in fitting the polymer/QD blend spectra.

C2. COMPARISON OF LONG-TIME TA SPECTRA (750 VS. 900 NM EXCITATION)

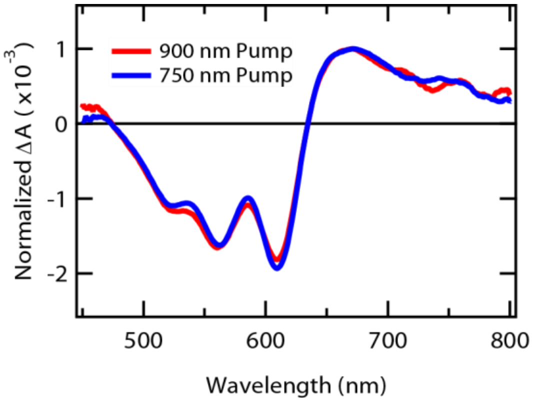

Figure C- 2. Comparison of TA spectra at ~1 ns time delay for a P3HT/PbS blend pumped at 750 nm (blue) and 900 nm (red), normalized at 670 nm.

C3. TRANSIENT ABSORPTION OF NEAT P3HT

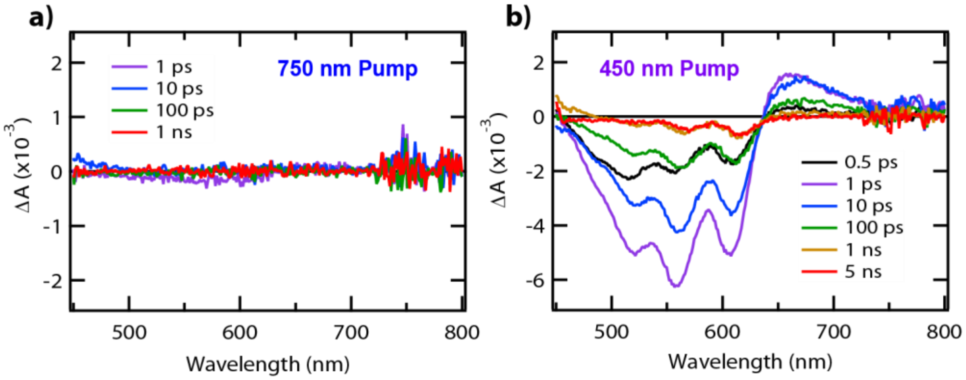

Figure C- 3. Transient absorption spectra of a neat P3HT film excited at (a) 750 nm and (b) 450 nm

We demonstrate that the 750 nm pump does not directly excite the polymer by verifying that a neat P3HT film does not exhibit TA signal when pumped at this wavelength, as shown in **Figure C- 1**a. The TA spectra resulting from direct excitation of the neat polymer at 450 nm is shown in **Figure C- 3**b.

C4. TRANSIENT ABSORPTION DATA FITS

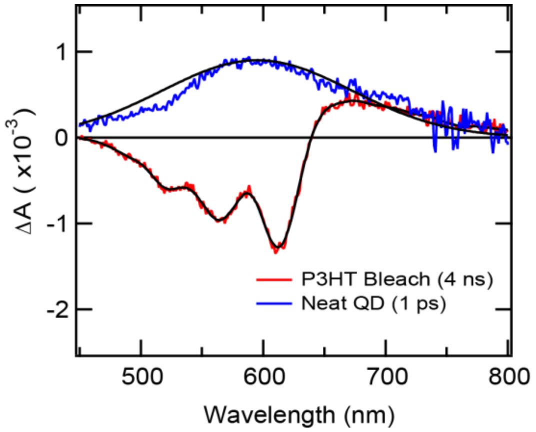

Figure C- 4. Fixed reference spectra used to fit the raw transient absorption data of the P3HT/PbS-QD blends. The polymer bleach is shown in red and overlaid with the smoothed spectrum in black; the quantum dot induced absorption feature is shown in blue, with the Gaussian approximation (black curve) for comparison.

The raw transient absorption data was approximated as a linear combination of two fixed reference spectra, representing the polymer bleach and QD induced absorption features shown in **Figure C- 4**. For the polymer reference spectrum, we used a spectral slice at ~4 ns time delay of the P3HT/PbS-QD blend excited at 750 nm, that was smoothed with a Savitzky-Golay algorithm in Igor Pro. At this time delay, the quantum dot PIA feature has fully decayed, leaving only signal from the long-lived polymer ground state bleach. The reference spectrum for the QD induced absorption feature was approximated with a Gaussian function, as smoothing the raw data introduced additional structure to the spectrum due to the low signal-to-noise ratio of the neat QD spectra collected with the same excitation intensities used for the polymer/QD blend TA experiments. Fits to individual spectra were obtained using a linear combination of the two fixed reference spectra according to the following expression:

$$\text{Fit}(\lambda) = \text{A*bleach}(\lambda) + \text{B*Gaussian}(\lambda)$$

where A and B are coefficients for the polymer (bleach) and QD (Gaussian) reference spectra, respectively. We minimized the sum of squared residuals between the fit and the raw spectra in the wavelength range of 450-800 nm by floating the A and B coefficients. This algorithm is performed for spectra at each time delay in a given data set, while tracking the fit coefficients. The kinetic data in **Figure 4-3** of the main text is generated by multiplying the polymer reference spectrum by its fitting coefficient (for each time delay) and plotting the resulting ΔA values of the ~610 nm feature as a function of time.

C5. EARLY TIMESCALE P3HT/PBS TA SPECTRA

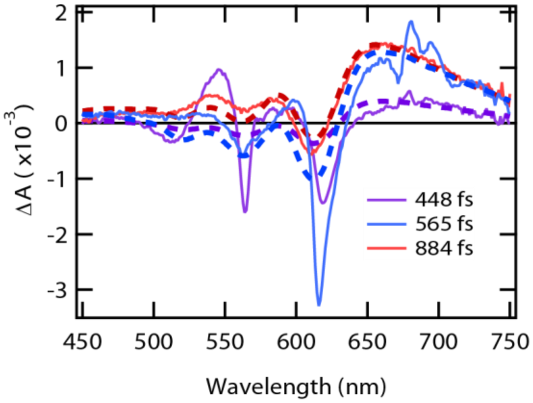

Figure C- 5. Early-time TA spectra of a P3HT/PbS film pumped at 750 nm. Dashed lines indicate fits to the data using the method described above.

C6. RAW TA DATA OF P3HT/PBS-QD BLENDS

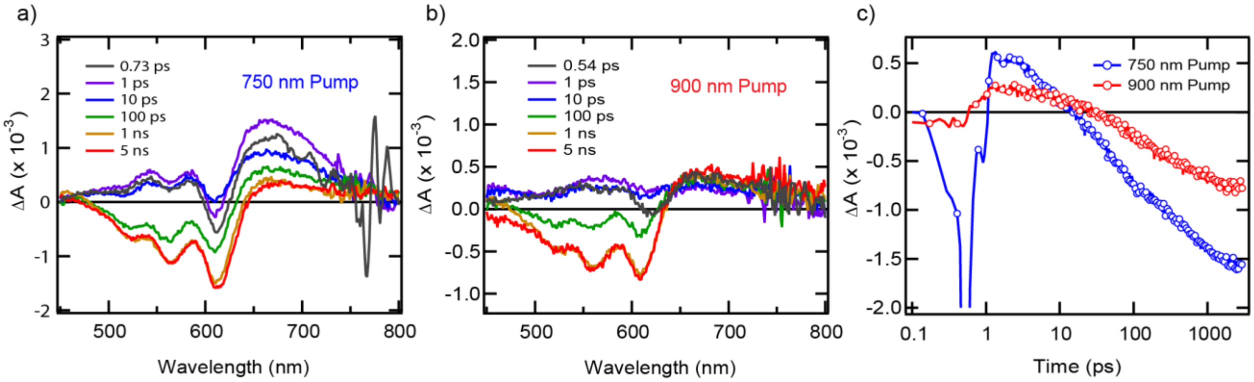

Figure C- 6. Raw transient absorption spectra of a P3HT/PbS-QD blend (postdeposition treated with TBAI) for (a) 750 nm and (b) 900 nm excitation, and (c) the corresponding kinetic traces of the polymer bleach feature at 610 nm.

REFERENCES

1. Key World Energy Statistics. 2015, Paris, France: International Energy Agency (IEA).

2. Tackling Challenges in Solar, 2014 Sunshot Initiative Portfolio, Us Department of Energy, DOE/EE-1081.

3. On the Path to Sunshot: The Role of Advancements in Solar Photovoltaic Efficiency, Reliability, and Costs. 2016, Golden, Co: National Renewable Energy Laboratory. NREL/TP-6A20-65872.

4. Battaglia, C.; Cuevas, A.; De Wolf, S. High-Efficiency Crystalline Silicon Solar Cells: Status and Perspectives. *Energ. Environ. Sci.* **2016**, *9*, 1552-1576.

5. Rauch, T.; Boberl, M.; Tedde, S. F.; Furst, J.; Kovalenko, M. V.; Hesser, G. N.; Lemmer, U.; Heiss, W.; Hayden, O. Near-Infrared Imaging with Quantum-Dot-Sensitized Organic Photodiodes. *Nat. Photonics* **2009**, *3*, 332-336.

6. Nanda, K. K.; Kruis, F. E.; Fissan, H.; Behera, S. N. Effective Mass Approximation for Two Extreme Semiconductors: Band Gap of PbS and CuBr Nanoparticles. *J. Appl. Phys.* **2004**, *95*, 5035-5041.

7. Hilczer, M.; Tachiya, M. Unified Theory of Geminate and Bulk Electron-Hole Recombination in Organic Solar Cells. *J. Phys. Chem. C* **2010**, *114*, 6808-6813.

8. Markov, D. E.; Amsterdam, E.; Blom, P. W. M.; Sieval, A. B.; Hummelen, J. C. Accurate Measurement of the Exciton Diffusion Length in a Conjugated Polymer Using a Heterostructure with a Side-Chain Cross-Linked Fullerene Layer. *J. Phys. Chem. A* **2005**, *109*, 5266-5274.

9. Sim, M.; Shin, J.; Shim, C.; Kim, M.; Jo, S. B.; Kim, J. H.; Cho, K. Dependence of Exciton Diffusion Length on Crystalline Order in Conjugated Polymers. *J. Phys. Chem. C* **2014**, *118*, 760-766.

10. Chang, Y. M.; Leu, C. Y. Conjugated Polyelectrolyte and Zinc Oxide Stacked Structure as an Interlayer in Highly Efficient and Stable Organic Photovoltaic Cells. *J. Mater. Chem. A* **2013**, *1*, 6446-6451.

11. He, Z. C.; Zhong, C. M.; Su, S. J.; Xu, M.; Wu, H. B.; Cao, Y. Enhanced Power-Conversion Efficiency in Polymer Solar Cells Using an Inverted Device Structure. *Nat. Photonics* **2012**, *6*, 591-595.

12. Greenham, N. C.; Peng, X. G.; Alivisatos, A. P. Charge Separation and Transport in Conjugated-Polymer/Semiconductor-Nanocrystal Composites Studied by Photoluminescence Quenching and Photoconductivity. *Phys. Rev. B* **1996**, *54*, 17628-17637.

13. Dayal, S.; Kopidakis, N.; Olson, D. C.; Ginley, D. S.; Rumbles, G. Photovoltaic Devices with a Low Band Gap Polymer and CdSe Nanostructures Exceeding 3% Efficiency. *Nano Lett.* **2010**, *10*, 239-242.

14. Kahmann, S.; Mura, A.; Protesescu, L.; Kovalenko, M. V.; Brabec, C. J.; Loi, M. A. Opto-Electronics of PbS Quantum Dot and Narrow Bandgap Polymer Blends. *J. Mater. Chem. C* **2015**, *3*, 5499-5505.

15. Dayal, S.; Reese, M. O.; Ferguson, A. J.; Ginley, D. S.; Rumbles, G.; Kopidakis, N. The Effect of Nanoparticle Shape on the Photocarrier Dynamics and Photovoltaic Device Performance of Poly(3-hexylthiophene):CdSe Nanoparticle Bulk Heterojunction Solar Cells. *Adv. Funct. Mater.* **2010**, *20*, 2629-2635.

16. Sun, B. Q.; Marx, E.; Greenham, N. C. Photovoltaic Devices Using Blends of Branched CdSe Nanoparticles and Conjugated Polymers. *Nano Lett.* **2003**, *3*, 961-963.

17. Noone, K. M.; Subramaniyan, S.; Zhang, Q. F.; Cao, G. Z.; Jenekhe, S. A.; Ginger, D. S. Photoinduced Charge Transfer and Polaron Dynamics in Polymer and Hybrid Photovoltaic Thin Films: Organic Vs Inorganic Acceptors. *J. Phys. Chem. C* **2011**, *115*, 24403-24410.

18. Lu, H.; Joy, J.; Gaspar, R. L.; Bradforth, S. E.; Brutchey, R. L. Iodide-Passivated Colloidal PbS Nanocrystals Leading to Highly Efficient Polymer:Nanocrystal Hybrid Solar Cells. *Chem. Mater.* **2016**, *28*, 1897-1906.

19. Piliego, C.; Manca, M.; Kroon, R.; Yarema, M.; Szendrei, K.; Andersson, M. R.; Heiss, W.; Loi, M. A. Charge Separation Dynamics in a Narrow Band Gap Polymer-PbS Nanocrystal Blend for Efficient Hybrid Solar Cells. *J. Mater. Chem.* **2012**, *22*, 24411-24416.

20. Seo, J.; Cho, M. J.; Lee, D.; Cartwright, A. N.; Prasad, P. N. Efficient Heterojunction Photovoltaic Cell Utilizing Nanocomposites of Lead Sulfide Nanocrystals and a Low-Bandgap Polymer. *Adv. Mater.* **2011**, *23,* 3984–3988.

21. Greaney, M. J.; Das, S.; Webber, D. H.; Bradforth, S. E.; Brutchey, R. L. Improving Open Circuit Potential in Hybrid P3HT:CdSe Bulk Heterojunction Solar Cells Via Colloidal Tert-Butylthiol Ligand Exchange. *ACS Nano* **2012**, *6*, 4222-4230.

22. Colbert, A. E.; Wu, W.; Janke, E. M.; Ma, F.; Ginger, D. S. Effects of Ligands on Charge Generation and Recombination in Hybrid Polymer/Quantum Dot Solar Cells. *J. Phys. Chem. C* **2015**, *119*, 24733-24739.

23. Zhou, R. J., et al. Enhancing the Efficiency of Solution-Processed Polymer:Colloidal Nanocrystal Hybrid Photovoltaic Cells Using Ethanedithiol Treatment. *ACS Nano* **2013**, *7*, 4846-4854.

24. Brown, P. R.; Kim, D.; Lunt, R. R.; Zhao, N.; Bawendi, M. G.; Grossman, J. C.; Bulović, V. Energy Level Modification in Lead Sulfide Quantum Dot Thin Films through Ligand Exchange. *ACS Nano* **2014**, *8*, 5863-5872.

25. Pattantyus-Abraham, A. G., et al. Depleted-Heterojunction Colloidal Quantum Dot Solar Cells. *ACS Nano* **2010**, *4*, 3374-3380.

26. Luther, J. M.; Gao, J. B.; Lloyd, M. T.; Semonin, O. E.; Beard, M. C.; Nozik, A. J. Stability Assessment on a 3% Bilayer PbS/Zno Quantum Dot Heterojunction Solar Cell. *Adv. Mater.* **2010**, *22*, 3704.

27. Choi, J. J., et al. PbSe Nanocrystal Excitonic Solar Cells. *Nano. Lett.* **2009**, *9*, 3749-3755.

28. Tang, J. et al. Colloidal-Quantum-Dot Photovoltaics Using Atomic-Ligand Passivation. *Nat. Mater.* **2011**, *10*, 765-771.

29. Chuang, C.-H. M.; Brown, P. R.; Bulović, V.; Bawendi, M. G. Improved Performance and Stability in Quantum dot Solar Cells through Band Alignment engineering. *Nat. Mater.* **2014**, *13*, 796-801.

30. Crisp, R. W.; Kroupa, D. M.; Marshall, A. R.; Miller, E. M.; Zhang, J. B.; Beard, M. C.; Luther, J. M. Metal Halide Solid-State Surface Treatment for High Efficiency PbS and PbSe QD Solar Cells. *Sci. Rep.* **2015**, *5*.

31. Ginger, D. S.; Greenham, N. C. Photoinduced Electron Transfer from Conjugated Polymers to CdSe Nanocrystals. *Phys. Rev. B* **1999**, *59*, 10622-10629.

32 Noone, K. M.; Strein, E.; Anderson, N. C.; Wu, P. T.; Jenekhe, S. A.; Ginger, D. S. Broadband Absorbing Bulk Heterojunction Photovoltaics Using Low-Bandgap Solution-Processed Quantum Dots. *Nano Lett.* **2010**, *10*, 2635-2639.

33. Strein, E.; Colbert, A.; Subramaniyan, S.; Nagaoka, H.; Schlenker, C. W.; Janke, E.; Jenekhe, S. A.; Ginger, D. S. Charge Generation and Energy Transfer in Hybrid Polymer/Infrared Quantum Dot Solar Cells. *Energ. Environ. Sci.* **2013**, *6*, 769-775.

34. Strein, E.; deQuilettes, D. W.; Hsieh, S. T.; Colbert, A. E.; Ginger, D. S. Hot Hole Transfer Increasing Polaron Yields in Hybrid Conjugated Polymer/PbS Blends. *J. Phys. Chem. Lett.* **2014**, *5*, 208-211.

35. ten Cate, S.; Schins, J. M.; Siebbeles, L. D. A. Origin of Low Sensitizing Efficiency of Quantum Dots in Organic Solar Cells. *ACS Nano* **2012**, *6*, 8983-8988.

36. Itskos, G.; Papagiorgis, P.; Tsokkou, D.; Othonos, A.; Hermerschmidt, F.; Economopoulos, S. P.; Yarema, M.; Heiss, W.; Choulis, S. Size-Dependent Charge Transfer in Blends of PbS Quantum Dots with a Low-Gap Silicon-Bridged Copolymer. *Adv. Energy Mater.* **2013**, *3*, 1490-1499.

37. Nagaoka, H.; Colbert, A. E.; Strein, E.; Janke, E. M.; Salvador, M.; Schlenker, C. W.; Ginger, D. S. Size-Dependent Charge Transfer Yields in Conjugated Polymer/Quantum Dot Blends. *J. Phys. Chem. C* **2014**, *118*, 5710-5715.

38. Liu, Z. K.; Sun, Y. X.; Yuan, J. Y.; Wei, H. X.; Huang, X. D.; Han, L.; Wang, W. W.; Wang, H. Q.; Ma, W. L. High-Efficiency Hybrid Solar Cells Based on Polymer/PbS_xSe_{1-X} Nanocrystals Benefiting from Vertical Phase Segregation. *Adv. Mater.* **2013**, *25*, 5772-5778.

39. Jarzab, D.; Szendrei, K.; Yarema, M.; Pichler, S.; Heiss, W.; Loi, M. A. Charge-Separation Dynamics in Inorganic-Organic Ternary Blends for Efficient Infrared Photodiodes. *Adv. Funct. Mater.* **2011**, *21*, 1988-1992.

40. Greaney, M. J.; Brutchey, R. L. Ligand Engineering in Hybrid Polymer:Nanocrystal Solar Cells. *Mater. Today* **2015**, *18*, 31–38.

41. Ip, A. H., et al. Hybrid Passivated Colloidal Quantum Dot Solids. *Nat. Nanotechnol.* **2012**, *7*, 577-582.

42. Zhitomirsky, D.; Voznyy, O.; Levina, L.; Hoogland, S.; Kemp, K. W.; Ip, A. H.; Thon, S. M.; Sargent, E. H. Engineering Colloidal Quantum Dot Solids within and Beyond the Mobility-Invariant Regime. *Nat. Commun.* **2014**, *5*.

43. Carey, G. H.; Abdelhady, A. L.; Ning, Z.; Thon, S. M.; Bakr, O. M.; Sargent, E. H. Colloidal Quantum Dot Solar Cells. *Chem. Rev.* **2015**, *115*, 12732–12763.

44. Szendrei, K.; Gomulya, W.; Yarema, M.; Heiss, W.; Loi, M. A. PbS Nanocrystal Solar Cells with High Efficiency and Fill Factor. *Appl. Phys. Lett.* **2010**, *97*.

45. Nagaoka, H.; Ma, F.; deQuilettes, D. W.; Vorpahl, S. M.; Glaz, M. S.; Colbert, A. E.; Ziffer, M. E.; Ginger, D. S. Zr Incorporation into TiO_2 Electrodes Reduces Hysteresis and Improves

Performance in Hybrid Perovskite Solar Cells While Increasing Carrier Lifetimes. *J. Phys. Chem. Lett.* **2015**, *6*, 669-675.

46. deQuilettes, D. W.; Vorpahl, S. M.; Stranks, S. D.; Nagaoka, H.; Eperon, G. E.; Ziffer, M. E.; Snaith, H. J.; Ginger, D. S. Impact of Microstructure on Local Carrier Lifetime in Perovskite Solar Cells. *Science* **2015**, *348*, 683-686.

47. Noone, K. M.; Anderson, N. C.; Horwitz, N. E.; Munro, A. M.; Kulkarni, A. P.; Ginger, D. S. Absence of Photoinduced Charge Transfer in Blends of PbSe Quantum Dots and Conjugated Polymers. *ACS Nano* **2009**, *3*, 1345-1352.

48. Hines, M. A.; Scholes, G. D. Colloidal PbS Nanocrystals with Size-Tunable near-Infrared Emission: Observation of Post-Synthesis Self-Narrowing of the Particle Size Distribution. *Adv. Mater.* **2003**, *15*, 1844-1849.

49. Liu, H., et al. Electron Acceptor Materials Engineering in Colloidal Quantum Dot Solar Cells. *Adv. Mater.* **2011**, *23*, 3832-3837.

50. Shuttle, C. G.; Maurano, A.; Hamilton, R.; O'Regan, B.; de Mello, J. C.; Durrant, J. R. Charge Extraction Analysis of Charge Carrier Densities in a Polythiophene/Fullerene Solar Cell: Analysis of the Origin of the Device Dark Current. *Appl. Phys. Lett.* **2008**, *93*.

51. Maurano, A.; Shuttle, C. G.; Hamilton, R.; Ballantyne, A. M.; Nelson, J.; Zhang, W. M.; Heeney, M.; Durrant, J. R. Transient Optoelectronic Analysis of Charge Carrier Losses in a Selenophene/Fullerene Blend Solar Cell. *J. Phys. Chem. C* **2011**, *115*, 5947-5957.

52. Knesting, K. M.; Ju, H. X.; Schlenker, C. W.; Giordano, A. J.; Garcia, A.; Smith, O. L.; Olson, D. C.; Marder, S. R.; Ginger, D. S. ITO Interface Modifiers Can Improve V_{oc} in Polymer Solar Cells and Suppress Surface Recombination. *J. Phys. Chem. Lett.* **2013**, *4*, 4038-4044.

53. Moreels, I., et al. Size-Dependent Optical Properties of Colloidal PbS Quantum Dots. *ACS Nano* **2009**, *3*, 3023-3030.

54. Jasieniak, J.; Califano, M.; Watkins, S. E. Size-Dependent Valence and Conduction Band-Edge Energies of Semiconductor Nanocrystals. *ACS Nano* **2011**, *5*, 5888-5902.

55 Zarghami, M. H.; Liu, Y.; Gibbs, M.; Gebremichael, E.; Webster, C.; Law, M. P-Type PbSe and PbS Quantum Dot Solids Prepared with Short-Chain Acids and Diacids. *ACS Nano* **2010**, *4*, 2475-2485.

56. Ning, Z. J.; Ren, Y.; Hoogland, S.; Voznyy, O.; Levina, L.; Stadler, P.; Lan, X. Z.; Zhitomirsky, D.; Sargent, E. H. All-Inorganic Colloidal Quantum Dot Photovoltaics Employing Solution-Phase Halide Passivation. *Adv. Mater.* **2012**, *24*, 6295-6299.

57. Jeong, K. S., et al. Enhanced Mobility-Lifetime Products in PbS Colloidal Quantum Dot Photovoltaics. *ACS Nano* **2012**, *6*, 89-99.

58. Cowan, S. R.; Roy, A.; Heeger, A. J. Recombination in Polymer-Fullerene Bulk Heterojunction Solar Cells. *Phys. Rev. B* **2010**, *82*, 245207.

59. Heinemann, M. D.; von Maydell, K.; Zutz, F.; Kolny-Olesiak, J.; Borchert, H.; Riedel, I.; Parisi, J. Photo-Induced Charge Transfer and Relaxation of Persistent Charge Carriers in Polymer/Nanocrystal Composites for Applications in Hybrid Solar Cells. *Adv. Funct. Mater.* **2009**, *19*, 3788-3795.

60. Nelson, J. *The Physics of Solar Cells*, 1 ed.; Imperial College Press: London, 2003, p 79-117.

61. Credgington, D.; Durrant, J. R. Insights from Transient Optoelectronic Analyses on the Open-Circuit Voltage of Organic Solar Cells. *J. Phys. Chem. Lett.* **2012**, *3*, 1465-1478.

62. Huynh, W. U.; Dittmer, J. J.; Alivisatos, A. P. Hybrid Nanorod-Polymer Solar Cells. *Science* **2002**, *295*, 2425-2427.

63. Sun, B.; Greenham, N. C. Improved Efficiency of Photovoltaics Based on CdSe Nanorods and Poly(3-Hexylthiophene) Nanofibers. *Phys. Chem. Chem. Phys.* **2006**, *8*, 3557-3560.

64. Itskos, G.; Othonos, A.; Rauch, T.; Tedde, S. F.; Hayden, O.; Kovalenko, M. V.; Heiss, W.; Choulis, S. A. Optical Properties of Organic Semiconductor Blends with near-Infrared Quantum-Dot Sensitizers for Light Harvesting Applications. *Adv. Energy Mater.* **2011**, *1*, 802-812.

65. Zhang, Y. G.; Li, Z.; Ouyang, J. Y.; Tsang, S. W.; Lu, J. P.; Yu, K.; Ding, J. F.; Tao, Y. Hole Transfer from PbS Nanocrystal Quantum Dots to Polymers and Efficient Hybrid Solar Cells Utilizing Infrared Photons. *Org. Electron.* **2012**, *13*, 2773-2780.

66. Xu, T. T.; Qiao, Q. Q. Conjugated Polymer-Inorganic Semiconductor Hybrid Solar Cells. *Energ. Environ. Sci.* **2011**, *4*, 2700-2720.

67. Subramaniyan, S.; Xin, H.; Kim, F. S.; Shoaee, S.; Durrant, J. R.; Jenekhe, S. A. Effects of Side Chains on Thiazolothiazole-Based Copolymer Semiconductors for High Performance Solar Cells. *Adv. Energy Mater.* **2011**, *1*, 854-860.

68. Subramaniyan, S.; Xin, H.; Kim, F. S.; Jenekhe, S. A. New Thiazolothiazole Copolymer Semiconductors for Highly Efficient Solar Cells. *Macromolecules* **2011**, *44*, 6245-6248.

69. Beek, W. J. E.; Wienk, M. M.; Janssen, R. A. J. Efficient Hybrid Solar Cells from Zinc Oxide Nanoparticles and a Conjugated Polymer. *Adv. Mater.* **2004**, *16*, 1009-1013.

70. Beek, W. J. E.; Wienk, M. M.; Kemerink, M.; Yang, X. N.; Janssen, R. A. J. Hybrid Zinc Oxide Conjugated Polymer Bulk Heterojunction Solar Cells. *J. Phys. Chem. B* **2005**, *109*, 9505-9516.

71. Sharma, S. N.; Vats, T.; Dhenadhayalan, N.; Ramamurthy, P.; Narula, A. K. Ligand-Dependent Transient Absorption Studies of Hybrid Polymer:CdSe Quantum Dot Composites. *Sol. Energ. Mat. Sol. C* **2012**, *100*, 6-15.

72. Ginger, D. S.; Greenham, N. C. Charge Injection and Transport in Films of CdSe Nanocrystals. *J. Appl. Phys.* **2000**, *87*, 1361-1368.

73. Luther, J. M.; Law, M.; Beard, M. C.; Song, Q.; Reese, M. O.; Ellingson, R. J.; Nozik, A. J. Schottky Solar Cells Based on Colloidal Nanocrystal Films. *Nano Lett.* **2008**, *8*, 3488-3492.

74. Koleilat, G. I.; Levina, L.; Shukla, H.; Myrskog, S. H.; Hinds, S.; Pattantyus-Abraham, A. G.; Sargent, E. H. Efficient, Stable Infrared Photovoltaics Based on Solution-Cast Colloidal Quantum Dots. *ACS Nano* **2008**, *2*, 833-840.

75. Ma, W.; Luther, J. M.; Zheng, H. M.; Wu, Y.; Alivisatos, A. P. Photovoltaic Devices Employing Ternary PbS_xSe_{1-X} Nanocrystals. *Nano Lett.* **2009**, *9*, 1699-1703.

76. Pacholski, C.; Kornowski, A.; Weller, H. Self-Assembly of Zno: From Nanodots, to Nanorods. *Angew. Chem. Int. Edit.* **2002**, *41*, 1188-1191.

77. Gao, J. B.; Perkins, C. L.; Luther, J. M.; Hanna, M. C.; Chen, H. Y.; Semonin, O. E.; Nozik, A. J.; Ellingson, R. J.; Beard, M. C. N-Type Transition Metal Oxide as a Hole Extraction Layer in PbS Quantum Dot Solar Cells. *Nano Lett.* **2011**, *11*, 3263-3266.

78. Ren, G. Q.; Schlenker, C. W.; Ahmed, E.; Subramaniyan, S.; Olthof, S.; Kahn, A.; Ginger, D. S.; Jenekhe, S. A. Photoinduced Hole Transfer Becomes Suppressed with Diminished Driving Force in Polymer-Fullerene Solar Cells While Electron Transfer Remains Active. *Adv. Funct. Mater.* **2013**, *23*, 1238-1249.

79. Hoke, E. T.; Vandewal, K.; Bartelt, J. A.; Mateker, W. R.; Douglas, J. D.; Noriega, R.; Graham, K. R.; Frechet, J. M. J.; Salleo, A.; McGehee, M. D. Recombination in Polymer:Fullerene Solar Cells with Open-Circuit Voltages Approaching and Exceeding 1.0 V. *Adv. Energy Mater.* **2013**, *3*, 220-230.

80. Kohler, A.; dos Santos, D. A.; Beljonne, D.; Shuai, Z.; Bredas, J. L.; Holmes, A. B.; Kraus, A.; Mullen, K.; Friend, R. H. Charge Separation in Localized and Delocalized Electronic States in Polymeric Semiconductors. *Nature* **1998**, *392*, 903-906.

81. Chan, W. L.; Ligges, M.; Jailaubekov, A.; Kaake, L.; Miaja-Avila, L.; Zhu, X. Y. Observing the Multiexciton State in Singlet Fission and Ensuing Ultrafast Multielectron Transfer. *Science* **2011**, *334*, 1541-1545.

82. Bakueva, L.; Musikhin, S.; Hines, M. A.; Chang, T. W. F.; Tzolov, M.; Scholes, G. D.; Sargent, E. H. Size-Tunable Infrared (1000-1600 nm) Electroluminescence from PbS Quantum-Dot Nanocrystals in a Semiconducting Polymer. *Appl. Phys. Lett.* **2003**, *82*, 2895-2897.

83. Choudhury, K. R.; Song, D. W.; So, F. Efficient Solution-Processed Hybrid Polymer-Nanocrystal near Infrared Light-Emitting Devices. *Org. Electron.* **2010**, *11*, 23-28.

84. Fokina, A.; Lee, Y.; Chang, J. H.; Braun, L.; Bae, W. K.; Char, K.; Lee, C.; Zentel, R. Side-Chain Conjugated Polymers for Use in the Active Layers of Hybrid Semiconducting Polymer/Quantum Dot Light Emitting Diodes. *Polym. Chem.* **2016**, *7*, 101-112.

85. Freitas, J. N.; Goncalves, A. S.; Nogueira, A. F. A Comprehensive Review of the Application of Chalcogenide Nanoparticles in Polymer Solar Cells. *Nanoscale* **2014**, *6*, 6371-6397.

86. Couderc, E.; Greaney, M. J.; Brutchey, R. L.; Bradforth, S. E. Direct Spectroscopic Evidence of Ultrafast Electron Transfer from a Low Band Gap Polymer to CdSe Quantum Dots in Hybrid Photovoltaic Thin Films. *J. Am. Chem. Soc.* **2013**, *135*, 18418-18426.

87. Hindson, J. C.; Saghi, Z.; Hernandez-Garrido, J. C.; Midgley, P. A.; Greenham, N. C. Morphological Study of Nanoparticle-Polymer Solar Cells Using High-Angle Annular Dark-Field Electron Tomography. *Nano Lett.* **2011**, *11*, 904-909.

88. Oosterhout, S. D.; Wienk, M. M.; van Bavel, S. S.; Thiedmann, R.; Koster, L. J. A.; Gilot, J.; Loos, J.; Schmidt, V.; Janssen, R. A. J. The Effect of Three-Dimensional Morphology on the Efficiency of Hybrid Polymer Solar Cells. *Nat. Mater.* **2009**, *8*, 818-824.

89. Jakowetz, A. C.; Böhm, M. L.; Zhang, J.; Sadhanala, A.; Huettner, S.; Bakulin, A. A.; Rao, A.; Friend, R. H. What Controls the Rate of Ultrafast Charge Transfer and Charge Separation Efficiency in Organic Photovoltaic Blends. *J. Am. Chem. Soc.* **2016**, *138*, 11672-11679.

90. Burke, T. M.; Sweetnam, S.; Vandewal, K.; McGehee, M. D. Beyond Langevin Recombination: How Equilibrium between Free Carriers and Charge Transfer States Determines the Open-Circuit Voltage of Organic Solar Cells. *Adv. Energy Mater.* **2015**, *5*, 1500123.

91. Grancini, G.; Maiuri, M.; Fazzi, D.; Petrozza, A.; Egelhaaf, H. J.; Brida, D.; Cerullo, G.; Lanzani, G. Hot Exciton Dissociation in Polymer Solar Cells. *Nat. Mater.* **2013**, *12*, 29-33.

92. Vandewal, K., et al. Efficient Charge Generation by Relaxed Charge-Transfer States at Organic Interfaces. *Nat. Mater.* **2014**, *13*, 63-68.

93. Colbert, A. E.; Janke, E. M.; Hsieh, S. T.; Subramaniyan, S.; Schlenker, C. W.; Jenekhe, S. A.; Ginger, D. S. Hole Transfer from Low Band Gap Quantum Dots to Conjugated Polymers in Organic/Inorganic Hybrid Photovoltaics. *J Phys Chem Lett* **2013**, *4*, 280-284.

94. Dimitrov, S. D.; Bakulin, A. A.; Nielsen, C. B.; Schroeder, B. C.; Du, J. P.; Bronstein, H.; McCulloch, I.; Friend, R. H.; Durrant, J. R. On the Energetic Dependence of Charge Separation in Low-Band-Gap Polymer/Fullerene Blends. *J. Am. Chem. Soc.* **2012**, *134*, 18189-18192.

95. Bakulin, A. A.; Rao, A.; Pavelyev, V. G.; van Loosdrecht, P. H. M.; Pshenichnikov, M. S.; Niedzialek, D.; Cornil, J.; Beljonne, D.; Friend, R. H. The Role of Driving Energy and Delocalized States for Charge Separation in Organic Semiconductors. *Science* **2012**, *335*, 1340-1344.

96. Jailaubekov, A. E., et al. Hot Charge-Transfer Excitons Set the Time Limit for Charge Separation at Donor/Acceptor Interfaces in Organic Photovoltaics. *Nat. Mater.* **2013**, *12*, 66-73.

97. Park, S. H.; Roy, A.; Beaupre, S.; Cho, S.; Coates, N.; Moon, J. S.; Moses, D.; Leclerc, M.; Lee, K.; Heeger, A. J. Bulk Heterojunction Solar Cells with Internal Quantum Efficiency Approaching 100%. *Nat. Photonics* **2009**, *3*, 297-302.

98. Bartelt, J. A., et al. The Importance of Fullerene Percolation in the Mixed Regions of Polymer-Fullerene Bulk Heterojunction Solar Cells. *Adv. Energy Mater.* **2013**, *3*, 364-374.

99. Sambur, J. B.; Novet, T.; Parkinson, B. A. Multiple Exciton Collection in a Sensitized Photovoltaic System. *Science* **2010**, *330*, 63-66.

100. El-Ballouli, A. O.; Alarousu, E.; Usman, A.; Pan, J.; Bakr, O. M.; Mohammed, O. F. Real-Time Observation of Ultrafast Intraband Relaxation and Exciton Multiplication in PbS Quantum Dots. *ACS Photonics* **2014**, *1*, 285-292.

101. Tisdale, W. A.; Williams, K. J.; Timp, B. A.; Norris, D. J.; Aydil, E. S.; Zhu, X. Y. Hot-Electron Transfer from Semiconductor Nanocrystals. *Science* **2010**, *328*, 1543-1547.

102. Yang, Y.; Rodriguez-Cordoba, W.; Xiang, X.; Lian, T. Q. Strong Electronic Coupling and Ultrafast Electron Transfer between PbS Quantum Dots and TiO_2 Nanocrystalline Films. *Nano Lett.* **2012**, *12*, 303-309.

103. Canovas, E.; Wang, H.; Karakus, M.; Bonn, M. Hot Electron Transfer from PbSe Quantum Dots Molecularly Bridged to Mesoporous Tin and Titanium Oxide Films. *Chem. Phys.* **2016**, *471*, 54-58.

104. Pandey, A.; Guyot-Sionnest, P. Slow Electron Cooling in Colloidal Quantum Dots. *Science* **2008**, *322*, 929-932.

105. Schaller, R. D.; Pietryga, J. M.; Goupalov, S. V.; Petruska, M. A.; Ivanov, S. A.; Klimov, V. I. Breaking the Phonon Bottleneck in Semiconductor Nanocrystals Via Multiphonon Emission Induced by Intrinsic Nonadiabatic Interactions. *Phys. Rev. Lett.* **2005**, *95*, 196401.

106. Harbold, J. M.; Du, H.; Krauss, T. D.; Cho, K. S.; Murray, C. B.; Wise, F. W. Time-Resolved Intraband Relaxation of Strongly Confined Electrons and Holes in Colloidal PbSe Nanocrystals. *Phys. Rev. B* **2005**, *72*, 195312.

107. Guyot-Sionnest, P.; Wehrenberg, B.; Yu, D. Intraband Relaxation in CdSe Nanocrystals and the Strong Influence of the Surface Ligands. *J. Chem. Phys.* **2005**, *123*, 074709.

108. An, J. M.; Califano, M.; Franceschetti, A.; Zunger, A. Excited-State Relaxation in PbSe Quantum Dots. *J. Chem. Phys.* **2008**, *128*, 164720.

109. Efros, A. L.; Kharchenko, V. A.; Rosen, M. Breaking the Phonon Bottleneck in Nanometer Quantum Dots - Role of Auger-Like Processes. *Solid State Commun.* **1995**, *93*, 281-284.

110. Morgenstern, F. S. F.; Rao, A.; Bohm, M. L.; Kist, R. J. P.; Vaynzof, Y.; Greenham, N. C. Ultrafast Charge- and Energy-Transfer Dynamics in Conjugated Polymer: Cadmium Selenide Nanocrystal Blends. *ACS Nano* **2014**, *8*, 1647-1654.

111. Cademartiri, L.; Montanari, E.; Calestani, G.; Migliori, A.; Guagliardi, A.; Ozin, G. A. Size-Dependent Extinction Coefficients of PbS Quantum Dots. *J. Am. Chem. Soc.* **2006**, *128*, 10337-10346.

112. Guo, J. M.; Ohkita, H.; Benten, H.; Ito, S. Charge Generation and Recombination Dynamics in Poly(3-Hexylthiophene)/Fullerene Blend Films with Different Regioregularities and Morphologies. *J. Am. Chem. Soc.* **2010**, *132*, 6154-6164.

113. Marsh, R. A.; Hodgkiss, J. M.; Albert-Seifried, S.; Friend, R. H. Effect of Annealing on P3ht:Pcbm Charge Transfer and Nanoscale Morphology Probed by Ultrafast Spectroscopy. *Nano Lett.* **2010**, *10*, 923-930.

114. Gelinas, S.; Rao, A.; Kumar, A.; Smith, S. L.; Chin, A. W.; Clark, J.; van der Poll, T. S.; Bazan, G. C.; Friend, R. H. Ultrafast Long-Range Charge Separation in Organic Semiconductor Photovoltaic Diodes. *Science* **2014**, *343*, 512-516.
115. Schins, J. M.; Trinh, M. T.; Houtepen, A. J.; Siebbeles, L. D. A. Probing Formally Forbidden Optical Transitions in PbSe Nanocrystals by Time- and Energy-Resolved Transient Absorption Spectroscopy. *Phys. Rev. B* **2009**, *80*, 035323.
116. Nootz, G.; Padilha, L. A.; Olszak, P. D.; Webster, S.; Hagan, D. J.; Van Stryland, E. W.; Levina, L.; Sukhovatkin, V.; Brzozowski, L.; Sargent, E. H. Role of Symmetry Breaking on the Optical Transitions in Lead-Salt Quantum Dots. *Nano Lett.* **2010**, *10*, 3577-3582.
117. Provencher, F.; Berube, N.; Parker, A. W.; Greetham, G. M.; Towrie, M.; Hellmann, C.; Cote, M.; Stingelin, N.; Silva, C.; Hayes, S. C. Direct Observation of Ultrafast Long-Range Charge Separation at Polymer-Fullerene Heterojunctions. *Nat. Commun.* **2014**, *5*, 4288.
118. Tisdale, W. A.; Zhu, X. Y. Artificial Atoms on Semiconductor Surfaces. *P. Natl. Acad. Sci. USA* **2011**, *108*, 965-970.
119. Coffey, D. C.; Larson, B. W.; Hains, A. W.; Whitaker, J. B.; Kopidakis, N.; Boltalina, O. V.; Strauss, S. H.; Rumbles, G. An Optimal Driving Force for Converting Excitons into Free Carriers in Excitonic Solar Cells. *J. Phys. Chem. C* **2012**, *116*, 8916-8923.